

Eskesen, B., et al., 2023, Neoarchean synkinematic metamorphic peak in the Isua supracrustal belt (West Greenland): *Geology*, v. XX, p. XXX–XXX, <https://doi.org/10.1130/G51564.1>

## Supplemental Material

**Supplemental text.**

**Tables S1–S2.**

**Figures S1–S16.**

## Supplement text S1

This supplement is the text accompanying the subsequent tables and figures. It starts with some information about the thermodynamic database.

For the calculation of figure 3 and figure S12, an updated version of the database Jun92 (Berman 1988) was used. It contains solutions models for all relevant solid solutions such as garnet, plagioclase, white mica, biotite, and chlorite that are implemented and documented in the database when downloading theriak-domino software. For amphibole, we used the model of Mäder and Berman (1992) and Mäder et al. (1994). This model has symmetric implementations of Fe- and Mg-endmembers including Fe-Tschermakite which constitutes more than 75% of the amphibole composition. We find that this rather simple model reproduces assemblages and phase compositions rather well. Databases with more sophisticated solution models such as recent thermocalc databases building on Holland and Powell (2011) including e.g. the solution model of Green et al. (2016) for amphibole and Holland et al. (2021) for feldspar are surprisingly less successful. We speculate that the reason for this is the iron rich composition of our sample. While Mäder's model treats Fe and Mg symmetrically for all endmembers, more recent amphibole models focus very much on the Mg-rich side. Modern solution models have great advantages that Mäder's model is not capable of, e.g. the treatment of high-pressure endmembers, Ti-, or Fe<sup>3+</sup>-bearing endmembers and many more aspects, but for this Fe-rich bulk composition with a high Fe-Tschermakite-component in amphibole (implemented as endmember in Mäder's model, not in other's), we get the most reasonable results with the JUN92 database. Sample and garnets are very poor in Mn and we neglected this endmember. Both models (Fig. 3 and S12) assume water saturated conditions. Predicted temperatures of 550-600 C for the peak assemblage are in line with Ti-in biotite temperatures (Henry and Guidotti, 2002).

Figure S1: Location of study area in West Greenland (A), Tectonic sketch map of the Isua supracrustal belt (B), and geological map of the sampling area on the western flank of the belt (C). Figure is from Stüeken et al. (2021).

Figure S2A-F: Thin section photomicrographs (polarized and cross polarized light, respectively) of 6 thin sections taken with an Emspira digital microscope. Sections S2A-S2E correspond to sections S4A-F. Section S4F is the section shown in figure 1 (2 rectangles in the center are damage caused by laser; see S5 and S6)

Figure S3: Thin section photomicrographs of investigated sample. Each figure shows the domain in polarized (upper panel) and cross-polarized light. Figures S3A-S3E are indicated in figure 2, and figures S3F-S3H in figure S4.

S3A: Fine-grained, mylonitic banding in sample matrix. Middle part consists of ultra-thin quartz-rich and mica-rich bands with boudinated small amphibole (high relief minerals). Upper part contains more amphibole (orange in cross-polarized light). Lowermost domain is part of the elongated pressure shadow of garnet and displays a higher biotite-white mica ratio than the matrix.

S3B: Blow up of ultra-fine banding in matrix. Section was tilted to allow identification of white mica (Blue color in cross-polarized light). Note partly post-kinematic biotite (yellow to brown color in upper panel). Micrograph also shows how abundant in carbon the mica-rich domains are (black domains and spots in upper panel).



S3C: Lower part of micrograph shows foliated matrix similar to previous figures. Upper part is more amphibole-rich with shear bands cutting through amphibole.

S3D: Lowermost part of micrograph shows ribbon-shaped garnet with “inclusion trails” of quartz. Upper part shows amphibole porphyroblast that displays dynamic recrystallization and undulous extinction.

S3E: Blow up of ribbon-shaped garnet in figure S3D showing that garnet consists of numerous small grains. Quartz-rich matrix between garnet grains appears deformed indicating post-garnet deformation.

S3F: Large garnet grain showing features of both the smaller ribbon garnets and porphyroblasts. Garnet shows well-developed inclusion trails parallel to the E-W-oriented foliation and an overall somewhat elongated shape but is clearly euhedral. Rigid garnet is surrounded by deformed amphibole that is bent around the porphyroblast, clearly indicating post-garnet deformation.

S3G: Large amphibole crystal dissected by a shear band. Amphibole also shows fine carbon banding and inclusion trails. Hence, deformation took place before and after amphibole growth.

S3H: Domain in matrix that is affected by more intense retrogression. Biotite (brown in upper panel) and especially clinozoisite (elongated and colorless laths with random orientation in upper panel, yellowish in lower panel) are clearly post-kinematic.

Figure S4: Micro xrf maps of five further thin sections of the investigated sample. Maps are overlays from elements Al, Ca, and Fe. Garnet is reddish, mica-rich domains blue and quartz black. Amphibole is greenish and brownish, respectively, due to different color spreading as a result of slightly different signal ratios. Frames indicate high-resolution element maps obtained with the microprobe (red) and optical-microscope images (black) presented in subsequent supplementary material (S9, S10, S2F-2H).

Figures S5-6: LA-ICP-MS maps displaying major- and trace element distributions. Color scales were chosen to best represent intra-grain variability. Maps were acquired using a 60  $\mu\text{m}$  spot size, a scanning speed of 20  $\mu\text{m/s}$ , an ablation rate of 10 Hz, and an energy of 80  $\text{mJ/cm}^2$ . As an external reference, NIST 610 was used and the data was processed in the Iolite 3.2 software (Paton et al., 2011).

Figure S5: Element compositions for the porphyroblast in figure 1. Ca, Mg, and Mn show the same zoning as seen in the electron microprobe maps (Fig. S6). LREE is depleted in the core of the garnet with a slightly higher concentration near the rim. Going toward heavier REEs, a gradually stronger zonation is seen, reversing from Dy and onward, with HREE fractionating into the core. Scanning direction was left to right.

Figure S6: Element compositions for the ribbon-shaped garnets shown in Figure 1. Major element distribution resembles that of the electron microprobe maps (Fig. S7). LREE shows no fractionation in the garnet, whatsoever, while HREE + Y and Sc show fractionation into the garnet, where a slight enrichment is seen in the grains toward the center of the band. Scanning direction was up to down.

Figs. S7-S13: element maps obtained with the microprobe. Acceleration voltage is 15 KV, beam current is 50 nA and measuring time 100 ms/spot for all maps.

Figure S7: Element maps for Fe, Mg, Mn, Ca, and Al for the garnet porphyroblast shown in figure 2. Color lookups in all element maps (S6-S10) are spread to enhance contrast. In fact, thin veins showing Mn-enrichment in this figure are only somewhat higher in Mn than the ambient garnet and still considerably lower than other garnet cores we measured (table S1). We propose that the cut through the porphyroblast actually does not transect the chemical core of the crystal. Nevertheless, the figure clearly illustrates preserved growth zoning in garnet. Black inclusions in all figures indicate quartz, thus, inclusions are almost exclusively quartz. This is yet another argument that corruption of the isotopic age by dissolution of older or younger inclusions seems unlikely.

Figure S8: Element map of euhedral garnet porphyroblast in figures S2D/S4D with profile of spot analyses. This section cuts a little deeper into the core of the crystal as the section in figure S6 and the crystal shape and prograde zoning are even slightly better preserved.

Figure S9: Element map of elongated garnet shown in figures S2C/S4C. Garnet is cut by shear bands and we interpret this grain as a deformed former porphyroblast. Despite deformation, zoning is identical to the one observed in well-preserved porphyroblasts.

S10: Element maps of garnets shown in figures S2E/S4E. Garnets display inclusions trails parallel to the main foliation. Garnet in fig. S10A does not show signs of internal deformation, garnet in figure S10 B might be somewhat boudinaged. All garnets display zoning pattern identical to the one observed in other garnets.

S11: Element map including ribbon-shaped, poikiloblastic garnet in figures S2A/S4A. Garnet best visible in Mn image. Ribbon shows overall zoning pattern identical to other garnets. Some small garnet domains display increase of Mn towards grain boundaries, which we interpret as being related to retrogression (see figures S12 and S13).

Figure S12/S13: High-resolution element maps of small rim domain in figure 2 and figure S6. Garnet shows slight increase in Mn concentration towards rims, which we attribute to retrogression. Ribbon-shaped garnets, however, preserve growth zoning with a larger amplitude (Fig. S11). We speculate that the hand-picked garnet split (Split Grt 1 in table S2) contains a larger fraction of retrogressed garnet than splits from single crystals (Grt 2-7 in table S2).

Figure S14: Predicted mineral fractions along the pressure-temperature path shown in figure 3 (480 °C/ 6.5 kbar - 575 °C/ 7.5 kbar - 535 °C/ 5.5 kbar). Prograde and retrograde paths were divided into 50 and 25 even steps, respectively. After each step, newly formed garnet was removed from the bulk composition before the assemblage for the next point was calculated. This scheme corresponds to complete garnet fractionation during growth and the garnet line actually shows the cumulative amount of garnet that has formed up to the respective step. Mineral formulas have been normalized to 12 oxygen to allow for comparison of mineral modes. Dashed line indicates peak conditions. Garnet growth mainly happens at the expense of amphibole during prograde metamorphism. Garnet fractionation actually increases the stability field of amphibole compared to the phase diagram figure 3 as the effective bulk is shifted towards high Mg-Fe ratios. Hence, amphibole is probably stable towards higher temperatures than in figure 3 along a garnet-fractionating path. We favor a clockwise pressure-temperature loop, which is also in line with white mica consistently being aligned in the foliation while biotite is partly post-kinematic.

Abbreviations: am, amphibole; bt, biotite; grt, garnet; ilm. ilmenite; pl, plagioclase; qtz, quartz; sph, titanite; wm, potassic white mica.

Figure S15: (A) 3-point age regression line for one whole-rock split, one amphibole separate, and garnet split Grt 1 that was acquired from the crushed sample and is assumed to have higher content of retrogressed garnet. (B) 3-point regression line for one whole-rock split, one amphibole separate, and garnet split Grt 3 that was acquired from a euhedral garnet crystal. For all regression lines,  $2\sigma$  uncertainties are used, calculated initial values and ages are based on  $\lambda^{176}\text{Lu} = 1.867 \times 10^{-11} \text{ yr}^{-1}$  (Scherer et al. 2001; Söderlund et al., 2004).

Figure S16: Epsilon Hf versus age evolution diagram for bulk rock samples from the meta-turbidites of the Rosing (1999) type locality published in Hoffmann et al. (2010). Hafnium bulk rock isotope compositions overlap with the initial of the garnet regression line of this study at ca. 2600 Ma indicating that the garnets grew in a single peak metamorphic event after the sample developed rather undisturbed since the volcanic formation of the source material at 3780 Ma. If garnet relicts from early Archean metamorphic events would be preserved, they would shift the initial of the isochron to more radiogenic compositions and the garnets would likely plot above the evolution trend of bulk rock samples from the same locality.

Table S1: XRF-derived bulk composition of the sample (column “bulk”) and selected microprobe analyses of rock-forming minerals. For garnet, “p” indicates porphyroblast, “r” a ribbon-like garnet shape, and “ret” a retrogressed outer rim. Column “bulk input” shows simplified input composition for thermodynamic models in figures 3 and S14. For clinozoisite, Fe is assumed to be ferric. In thermodynamic models, xrf-measured ferric iron was assumed to be ferrous in the input bulk composition.

Table S2: Lu and Hf isotope data from a whole rock split, an amphibole separate, and garnet separates (Grt 1-7) used for the calculation of regression lines.

## Literature

Berman, R.G. (1988): Internally-Consistent Thermodynamic Data for Minerals in the System Na<sub>2</sub>O-K<sub>2</sub>O-CaO-MgO-FeO-Fe<sub>2</sub>O<sub>3</sub>-Al<sub>2</sub>O<sub>3</sub>-SiO<sub>2</sub>-TiO<sub>2</sub>-H<sub>2</sub>O-CO<sub>2</sub>. *Journal of Petrology*, Volume 29, Issue 2, 445–522. <https://doi.org/10.1093/petrology/29.2.445>.

Green, E.C.R, White, R.W., Diener, J.F.A., Powell, R., Holland, T.J.B. and Palin, R.M. (2016): Activity-composition relations for the calculation of partial melting equilibria in metabasic rocks. *Journal of Metamorphic Geology*, 34, 845-869. doi:10.1111/jmg.12211.

Henry, D.J., and Guidotti, C.V.G. (2002): Titanium in biotite from metapelitic rocks: Temperature effects, crystal-chemical controls and petrologic applications. *American Mineralogist*, 87, 375-382.

Hoffmann, J.E., Münker, C., Polat A., König, S., Mezger, K., Rosing, M.T. (2010): Highly depleted Hadean mantle reservoirs in the sources of early Archean arc-like rocks, Isua, SW-Greenland. *Geochimica et Cosmochimica Acta* 74(24), 7236–7260. DOI: [10.1016/j.gca.2010.09.027](https://doi.org/10.1016/j.gca.2010.09.027)

Holland, T.J.B. and Powell, R. (2011): An improved and extended internally consistent thermodynamic dataset for phases of petrological interest, involving a new equation of state for solids. *Journal of Metamorphic Geology*, 29, 333-383.

Holland, T.J.B., Green, E.C.R. and Powell, R. (2021): A thermodynamic model for feldspars in  $\text{KAlSi}_3\text{O}_8$ - $\text{NaAlSi}_3\text{O}_8$ - $\text{CaAl}_2\text{Si}_2\text{O}_8$  for mineral equilibrium calculations. *Journal of Metamorphic Geology*, 1-14. doi:10.1111/jmg.12639

Mäder, U. K., and Berman, R. G. (1992): Amphibole thermobarometry, a thermodynamic approach, in *Current research, Part E: Geological Survey of Canada Paper 92-1E*, p. 393–400.

Mäder, U. K., Percival, J. A., and Berman, R. G. (1994): Thermobarometry of garnet-clinopyroxene-hornblende granulites from the Kapuskasing structural zone: *Canadian Journal of Earth Sciences*, v. 31, p. 1134–1145.

Paton C, Hellstrom J, Paul B, Woodhead J, Hergt J (2011) *Iolite*: Freeware for the visualisation and processing of mass spectrometric data. *J Anal Atom Spectrom* 26(12):2508–2518. <https://doi.org/10.1039/c1ja10172b>

Söderlund, U, Patchett, PJ, Vervoort, JD, Isachsen, CE (2004): The  $^{176}\text{Lu}$  decay constant determined by Lu-Hf and U- Pb isotope systematics of Precambrian mafic intrusions. *Earth and Planetary Science Letters*, 219, 311–324.

Stüeken, E.E., Boocock T., Szilas K., Mikhail S. and Gardiner N.J. (2021): Reconstructing Nitrogen Sources to Earth's Earliest Biosphere at 3.7 Ga. *Front. Earth Sci.* 9:675726. doi: 10.3389/feart.2021.675726.

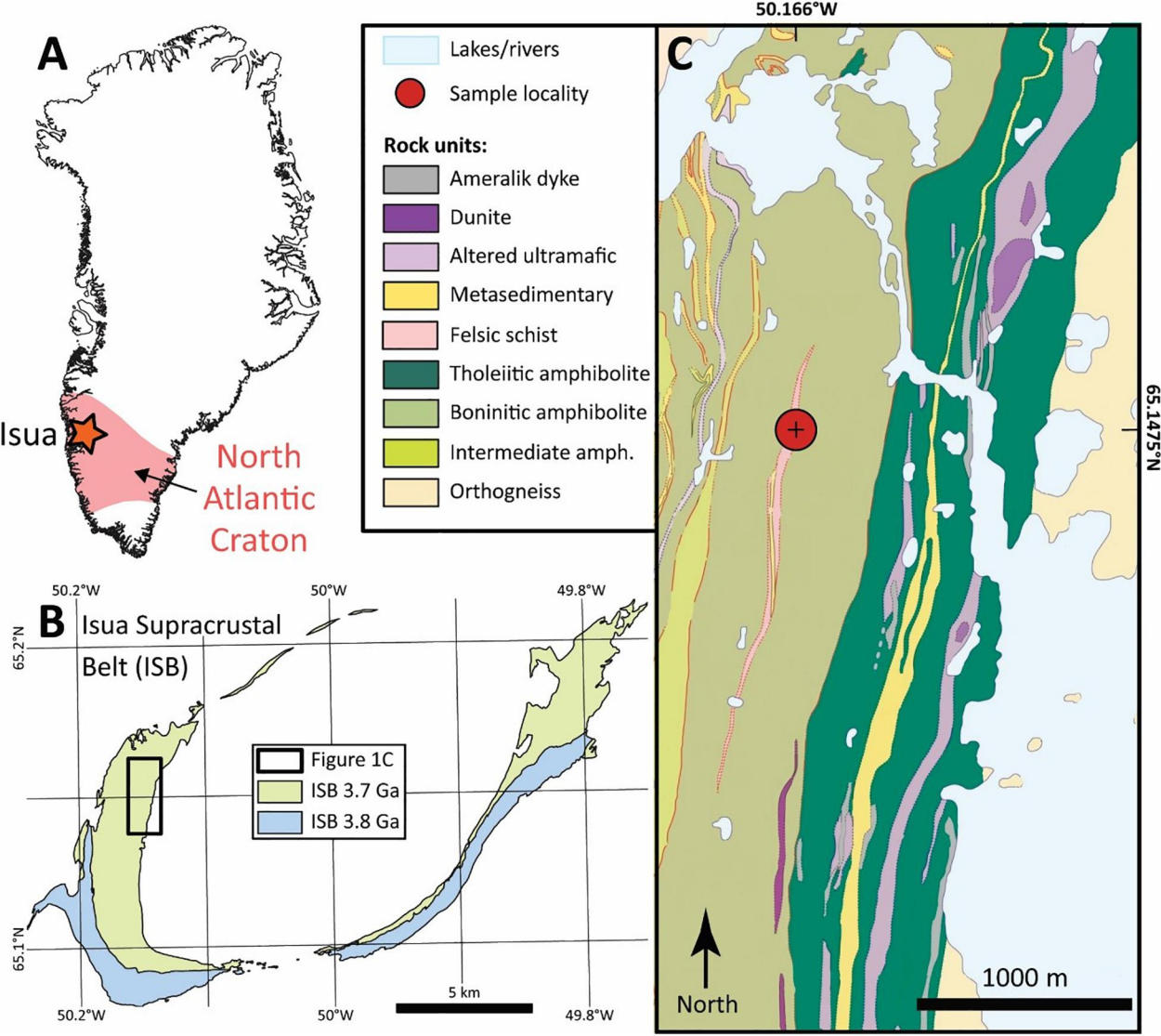




Fig. S2 A

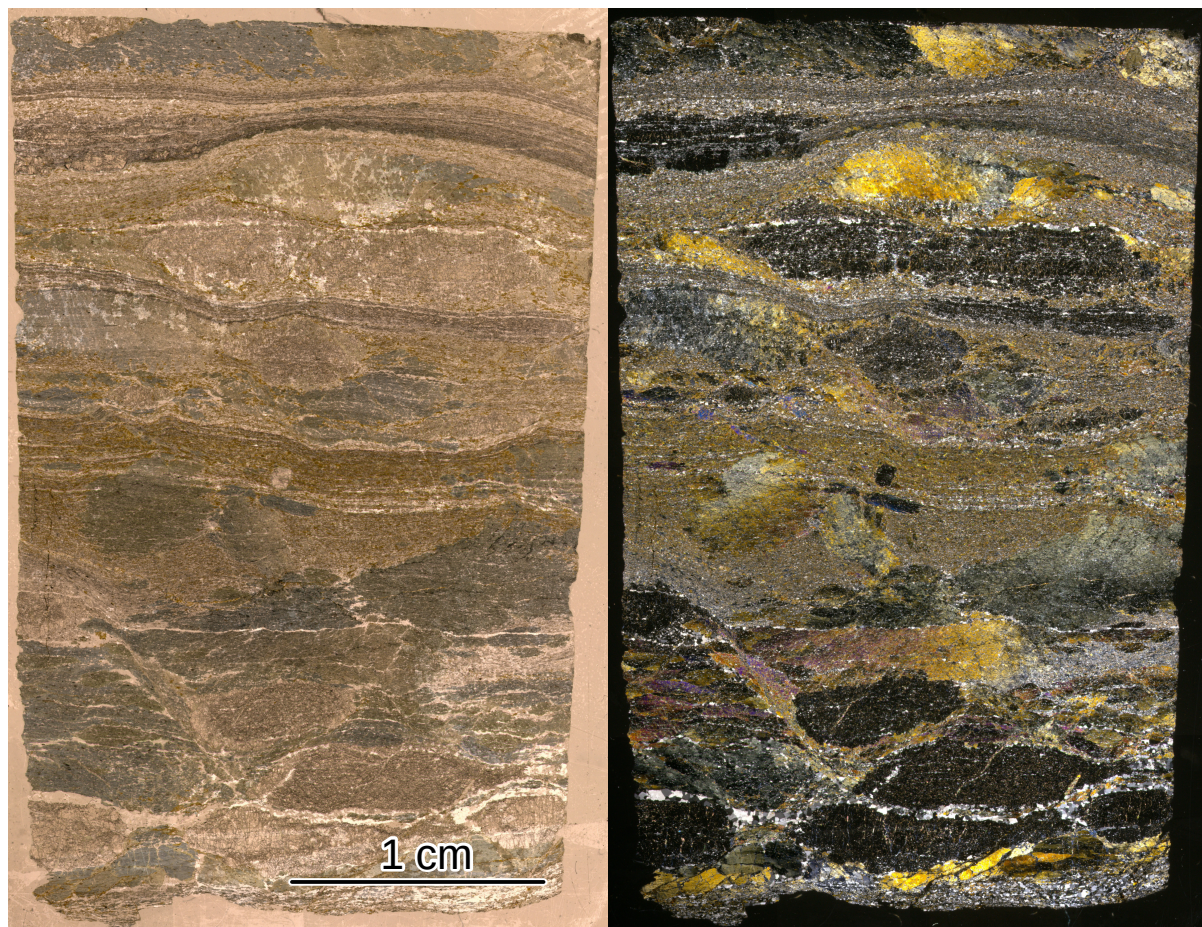




Fig. S2 B

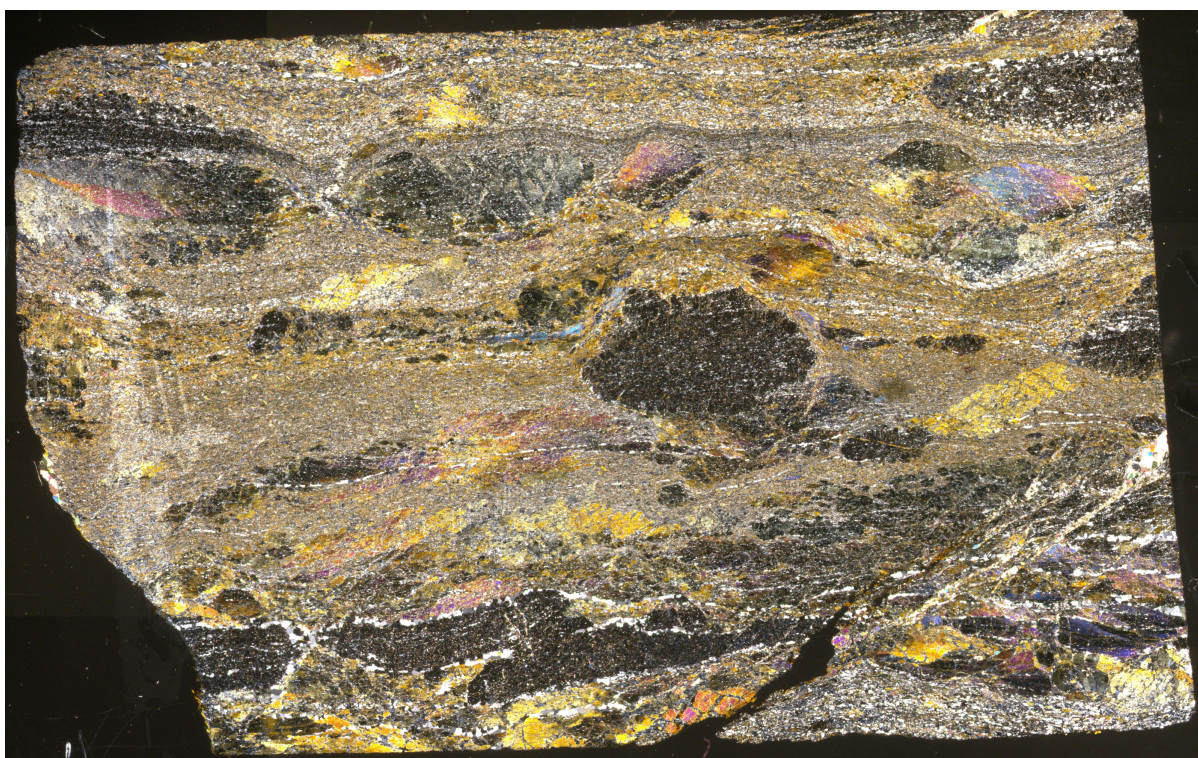
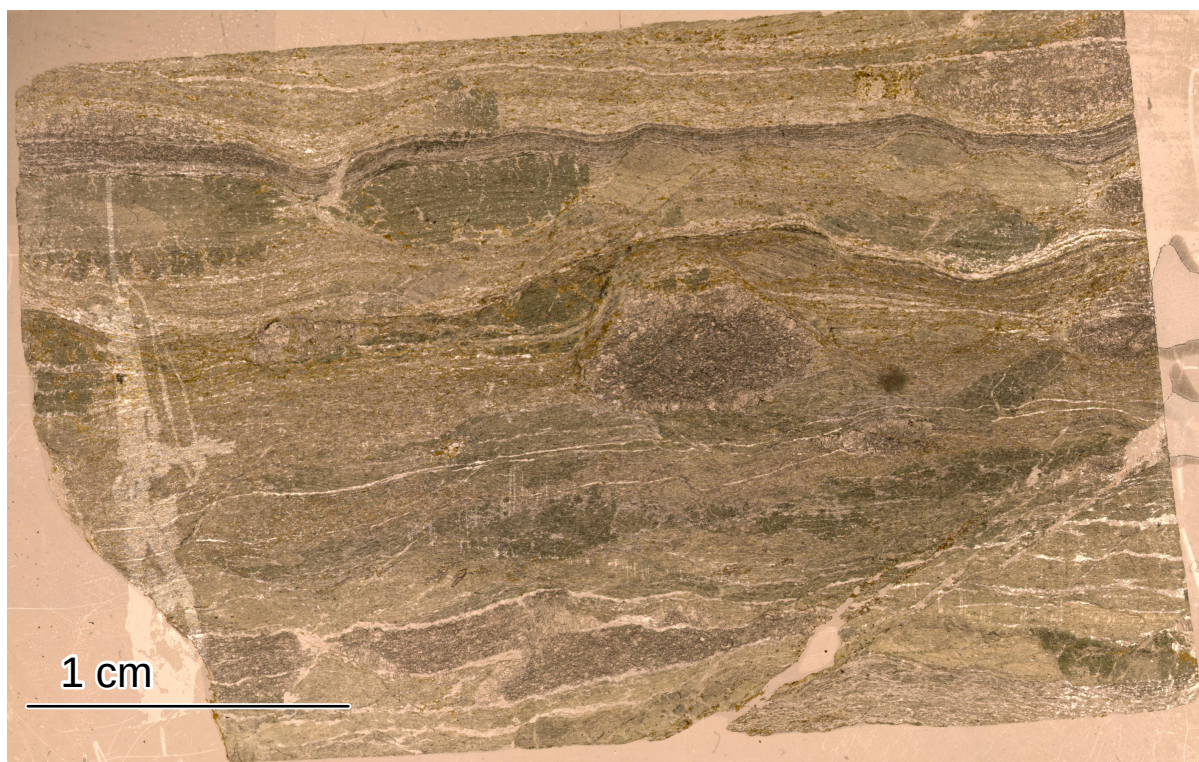




Fig. S2 C

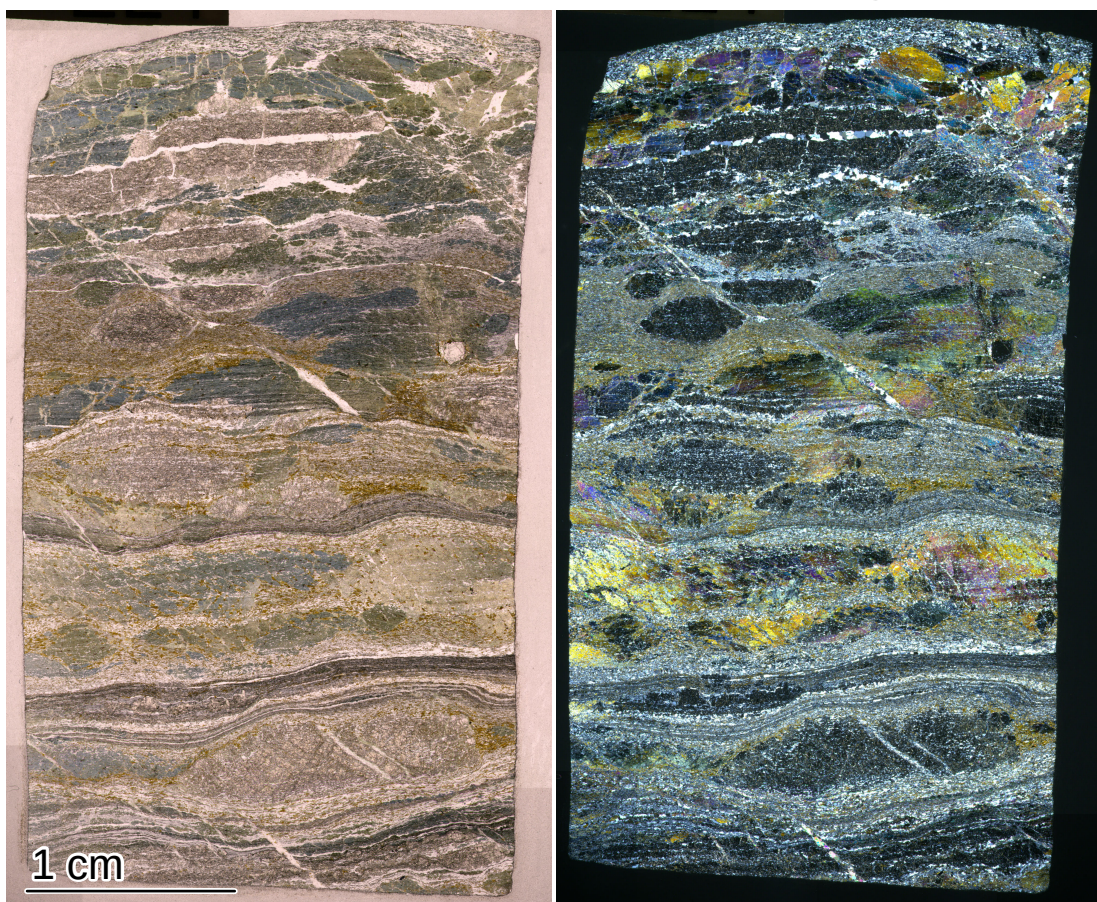




Fig. S2 D

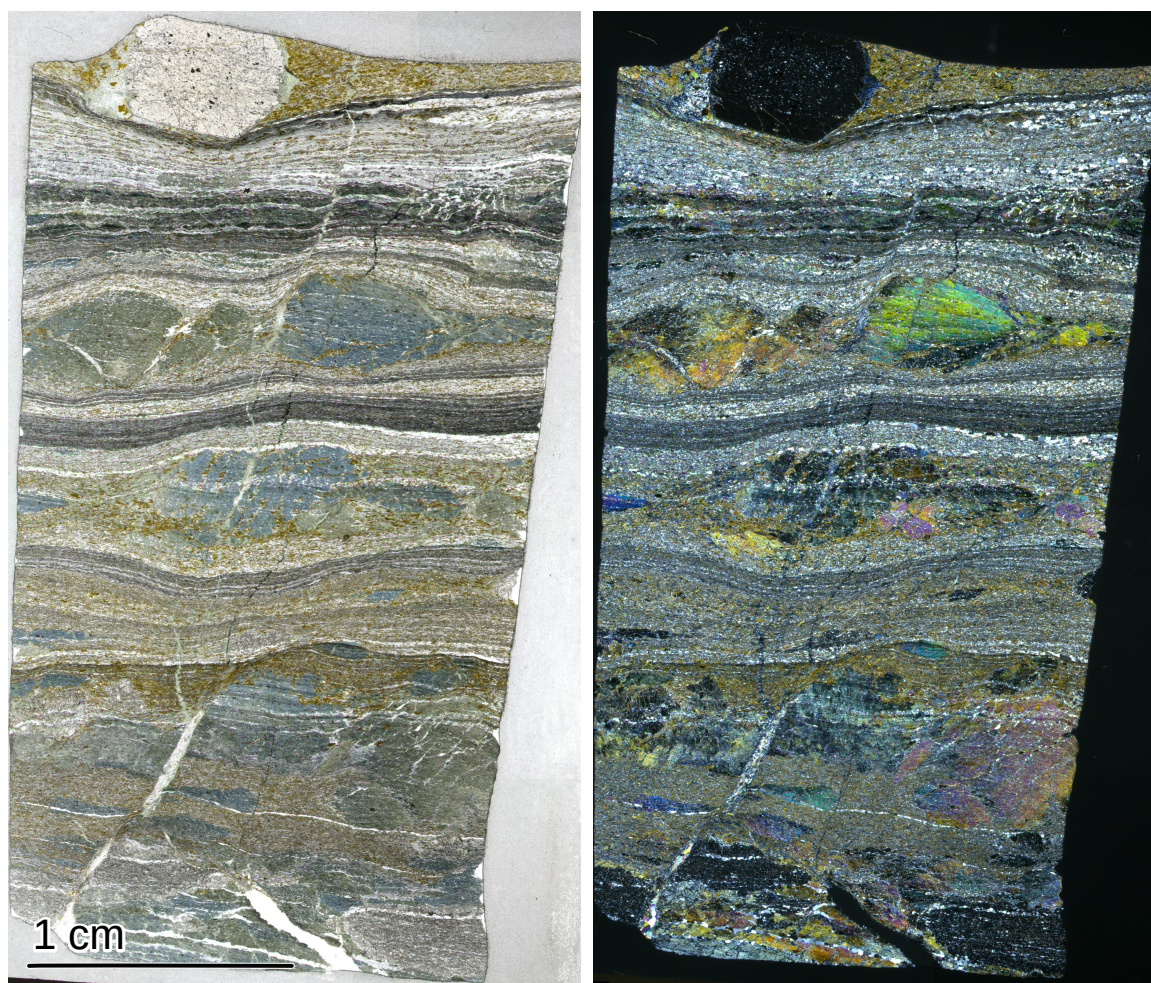




Fig. S2 E

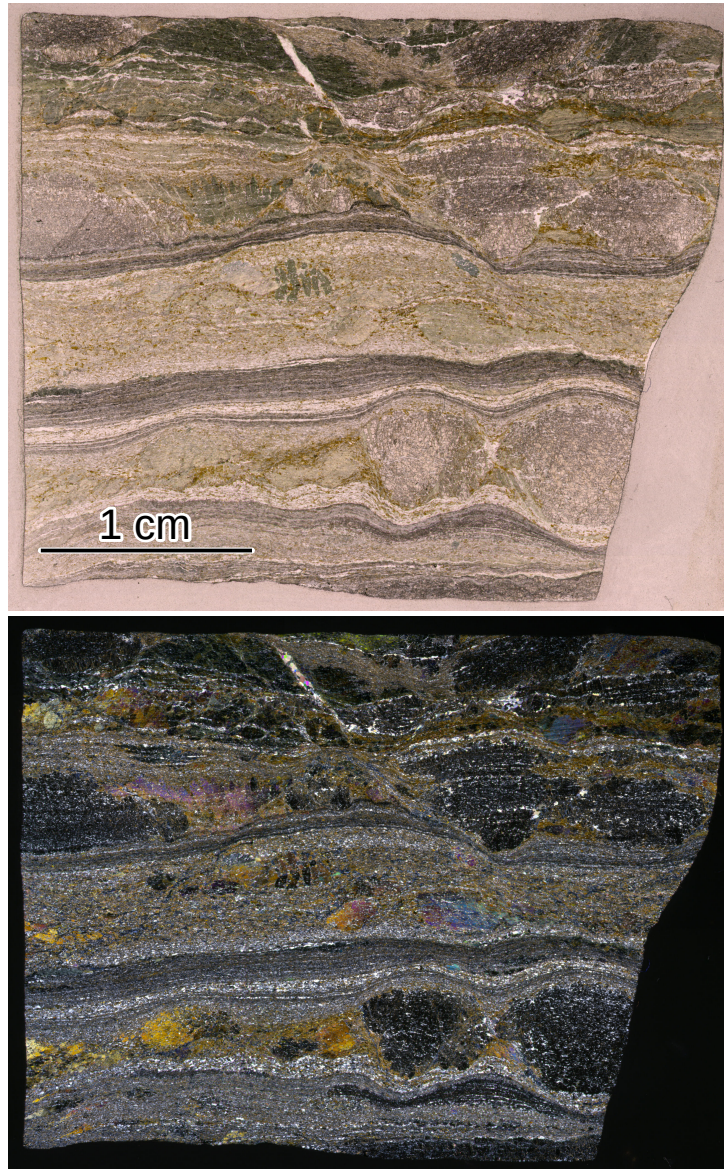
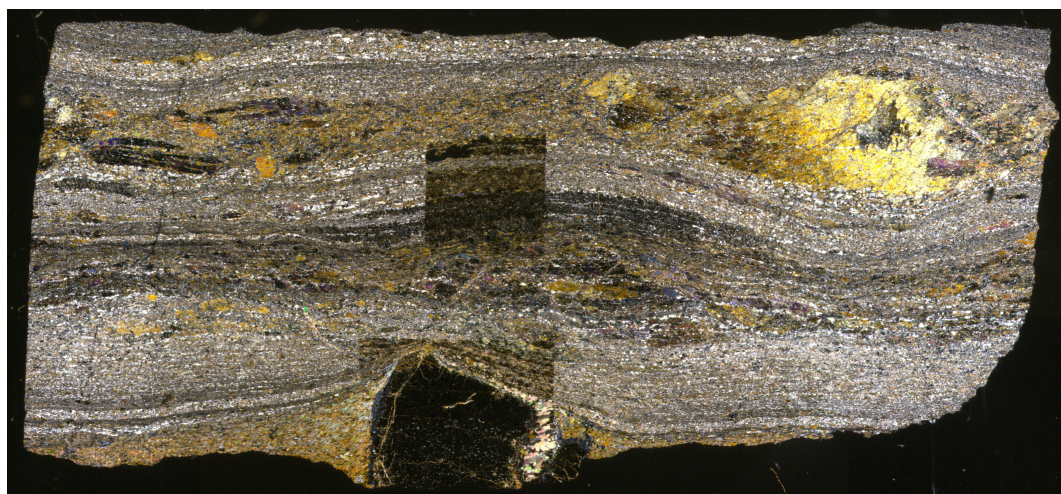
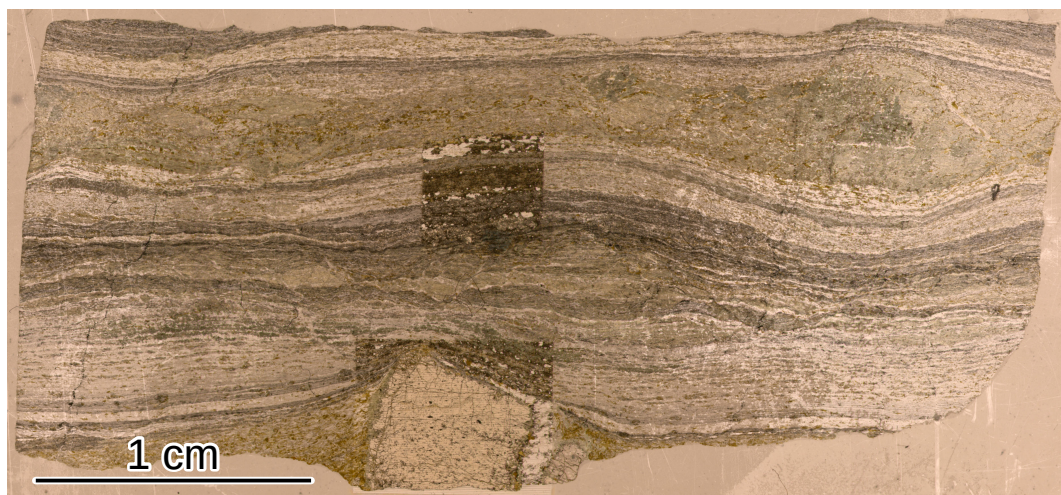
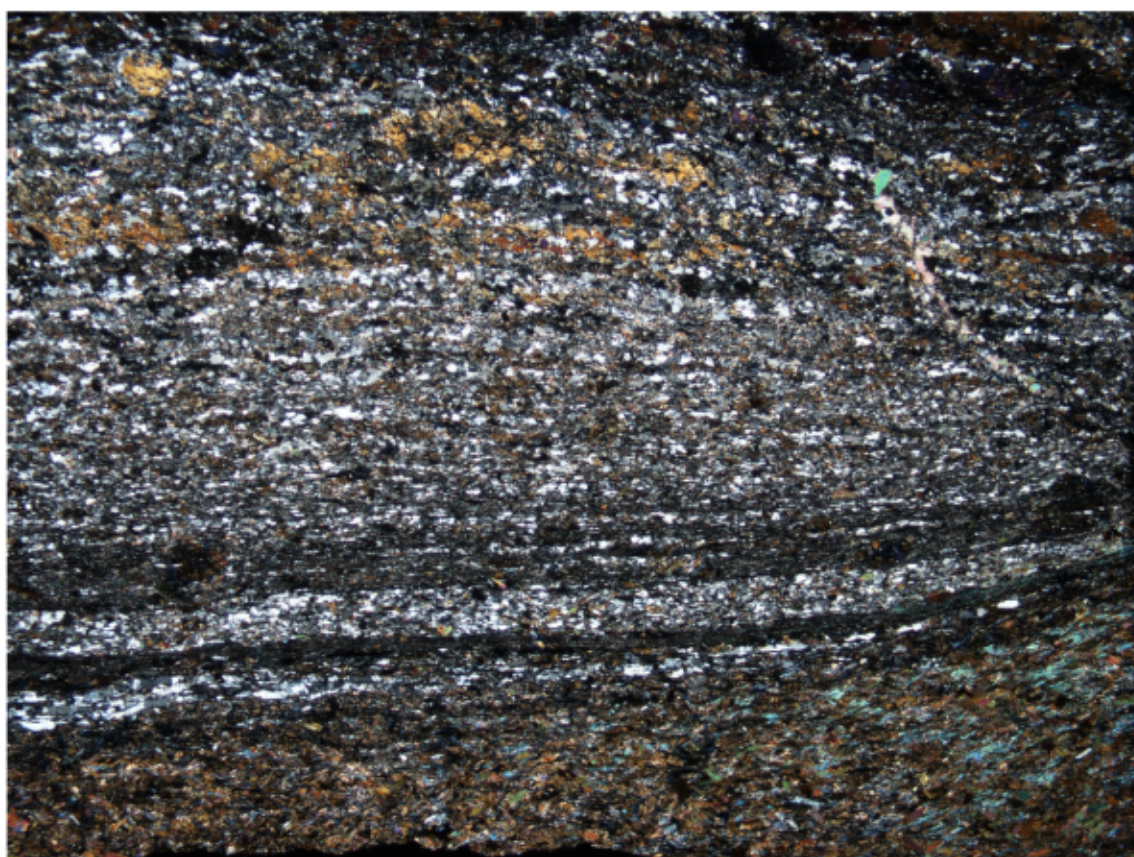
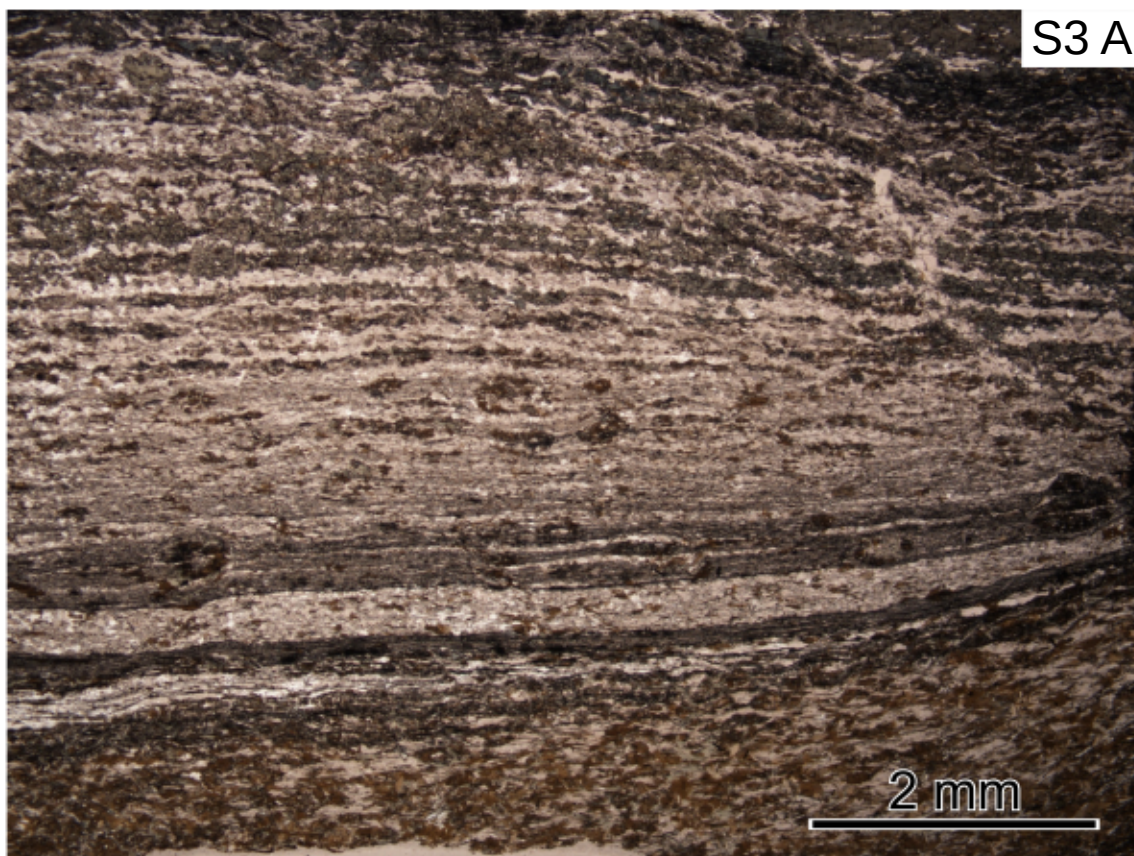




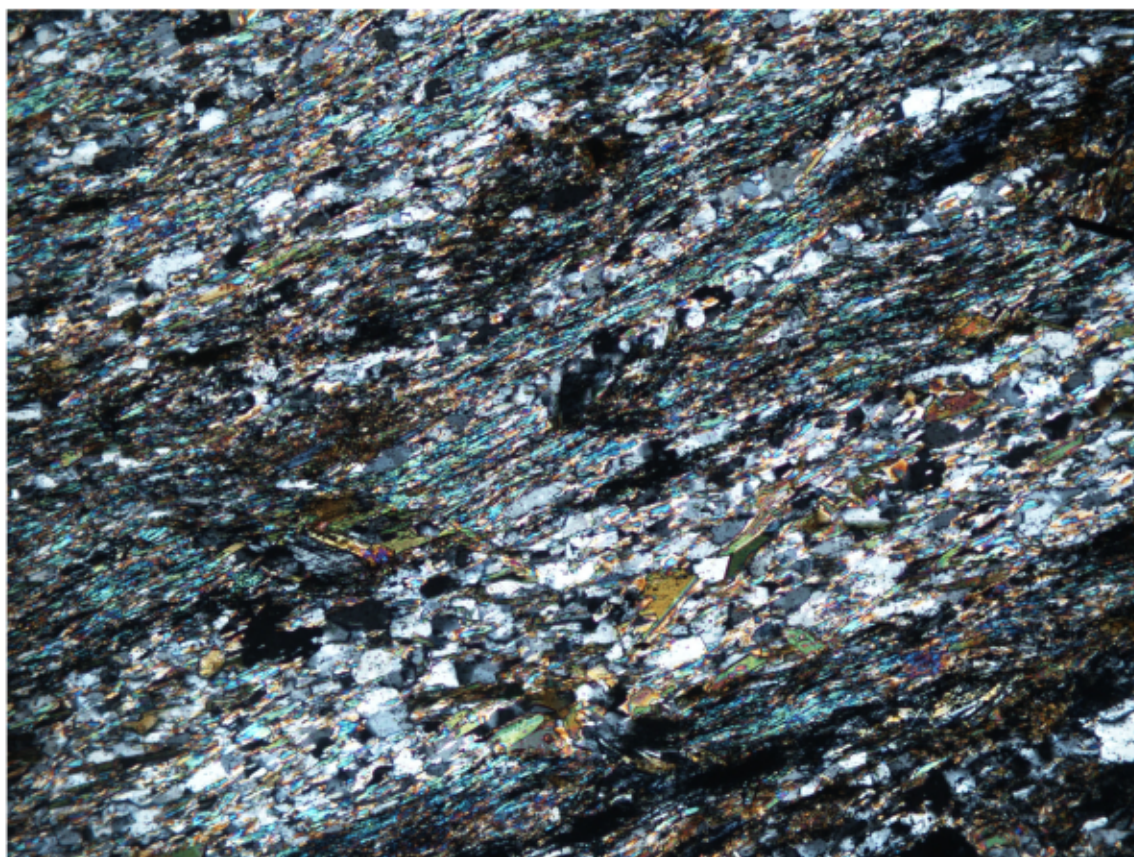
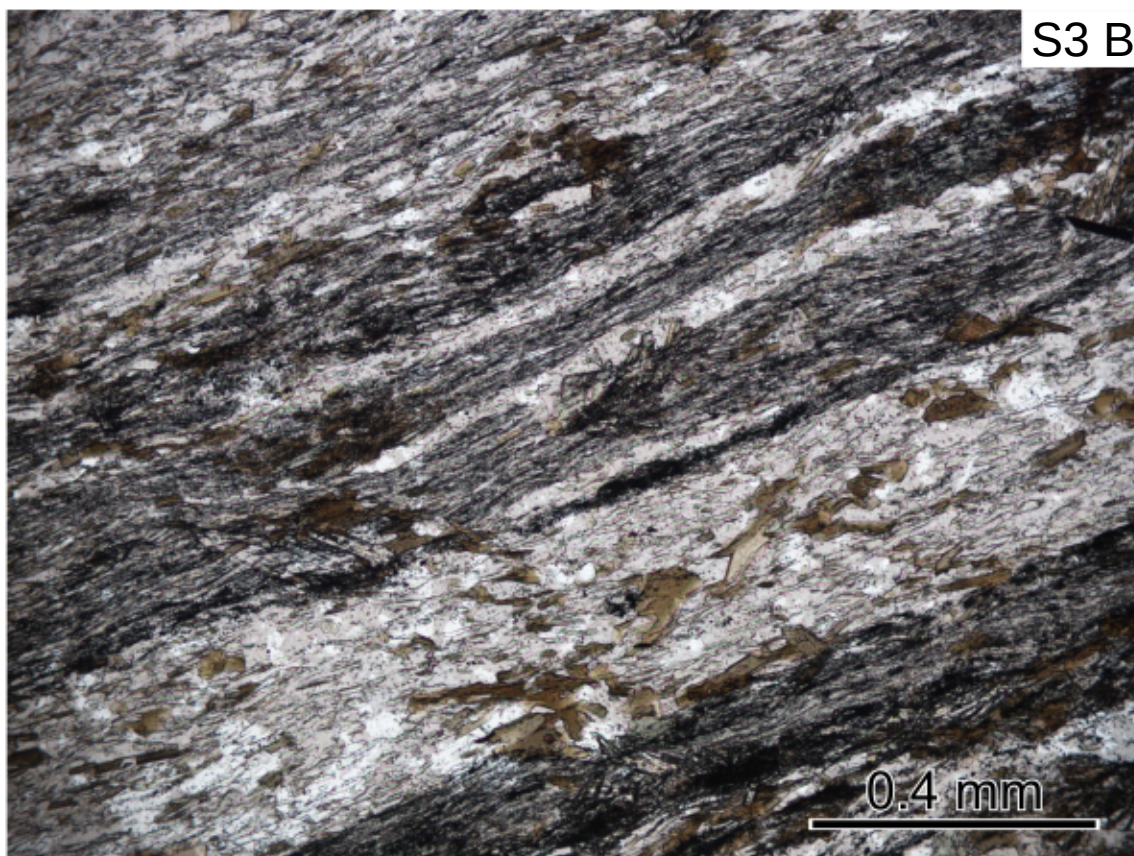
Fig. S2 F



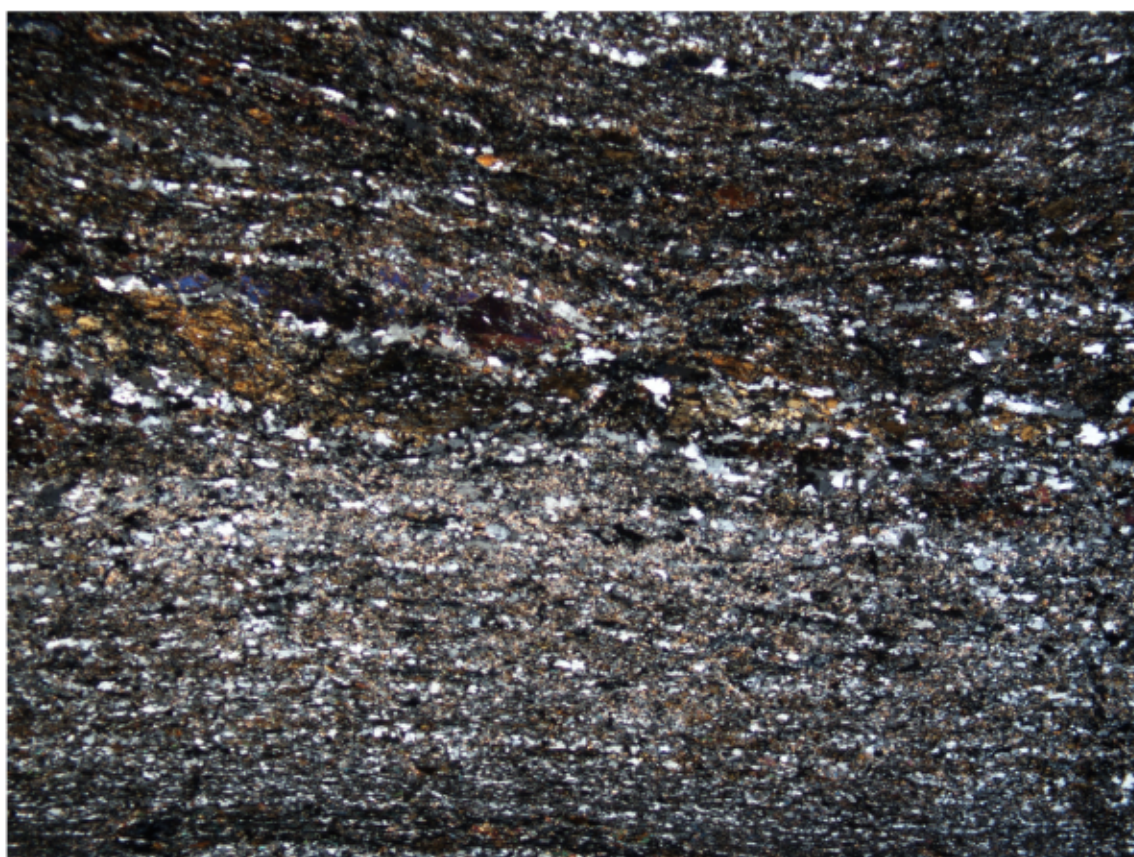
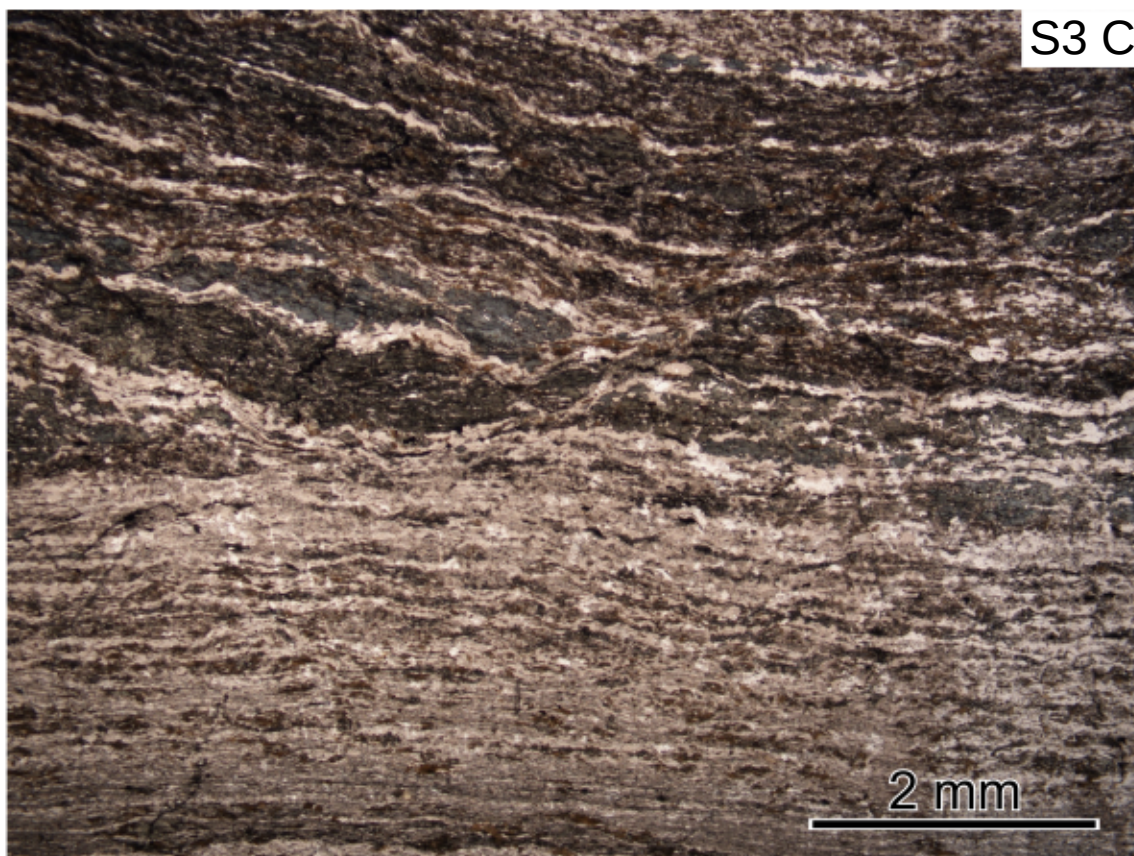




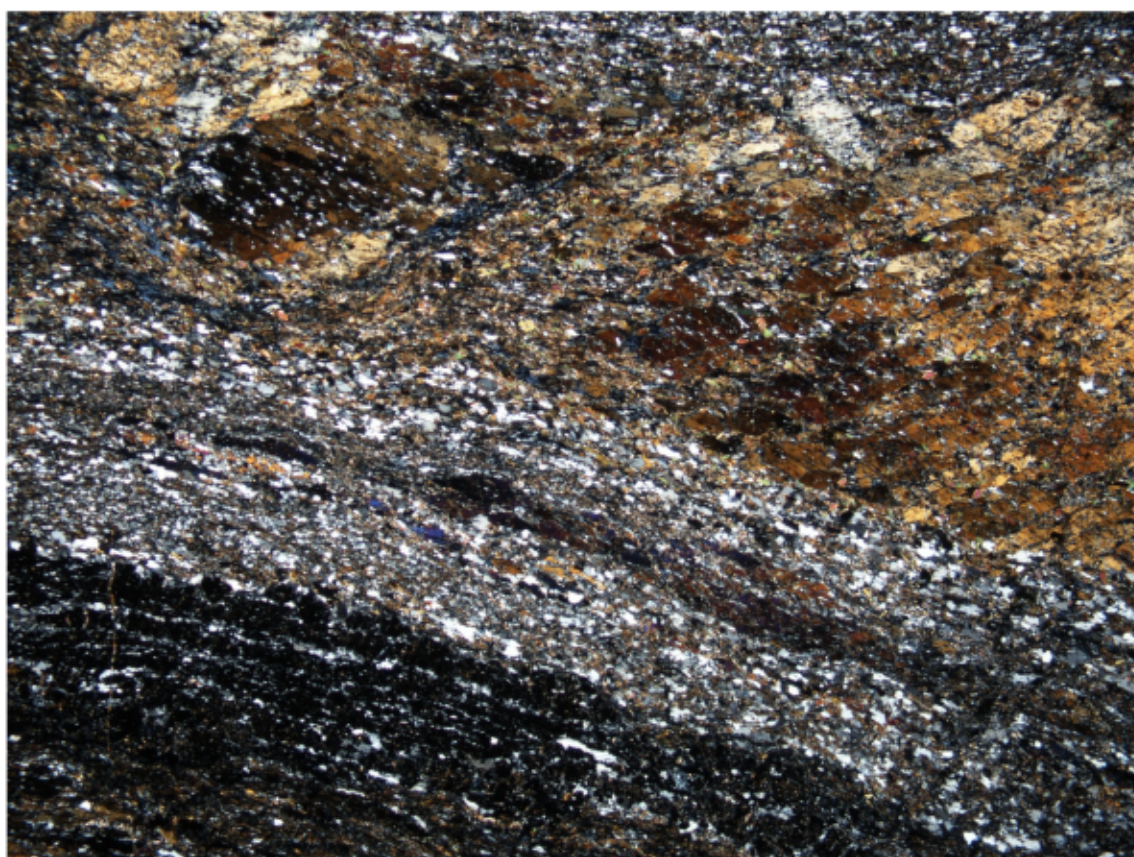




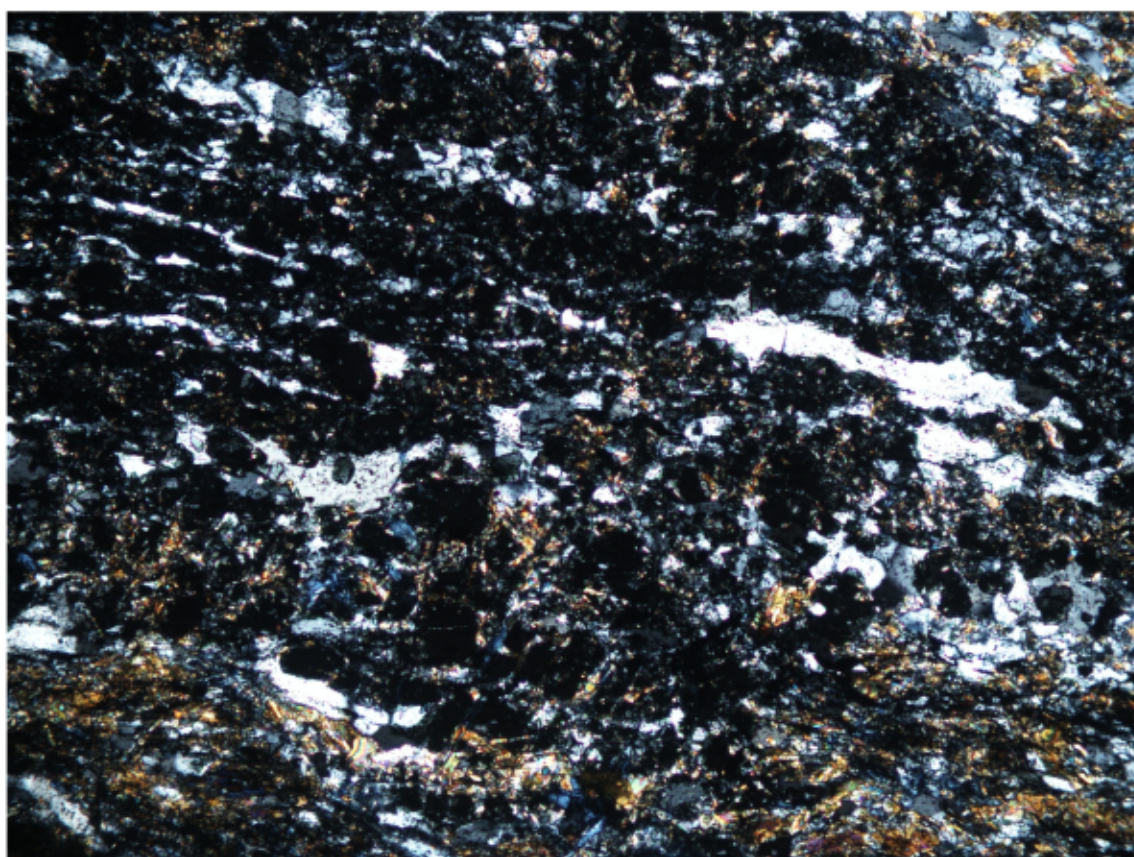
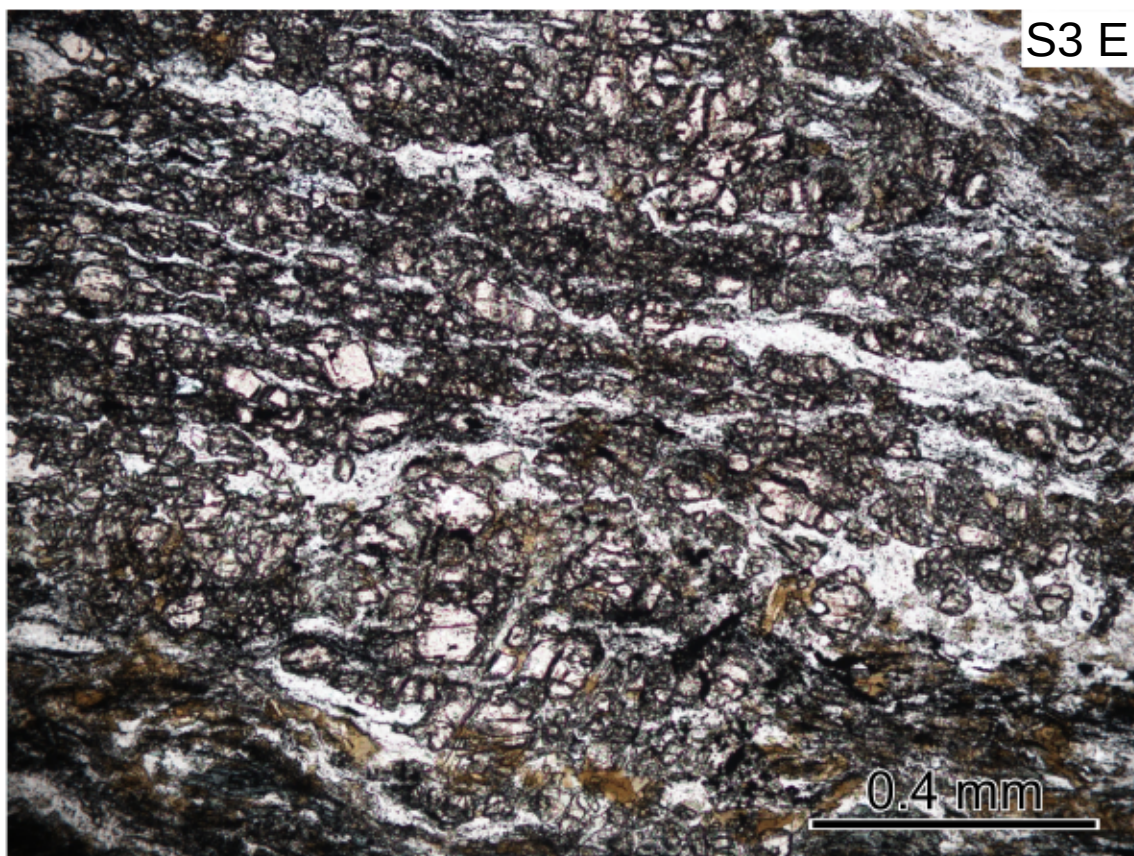




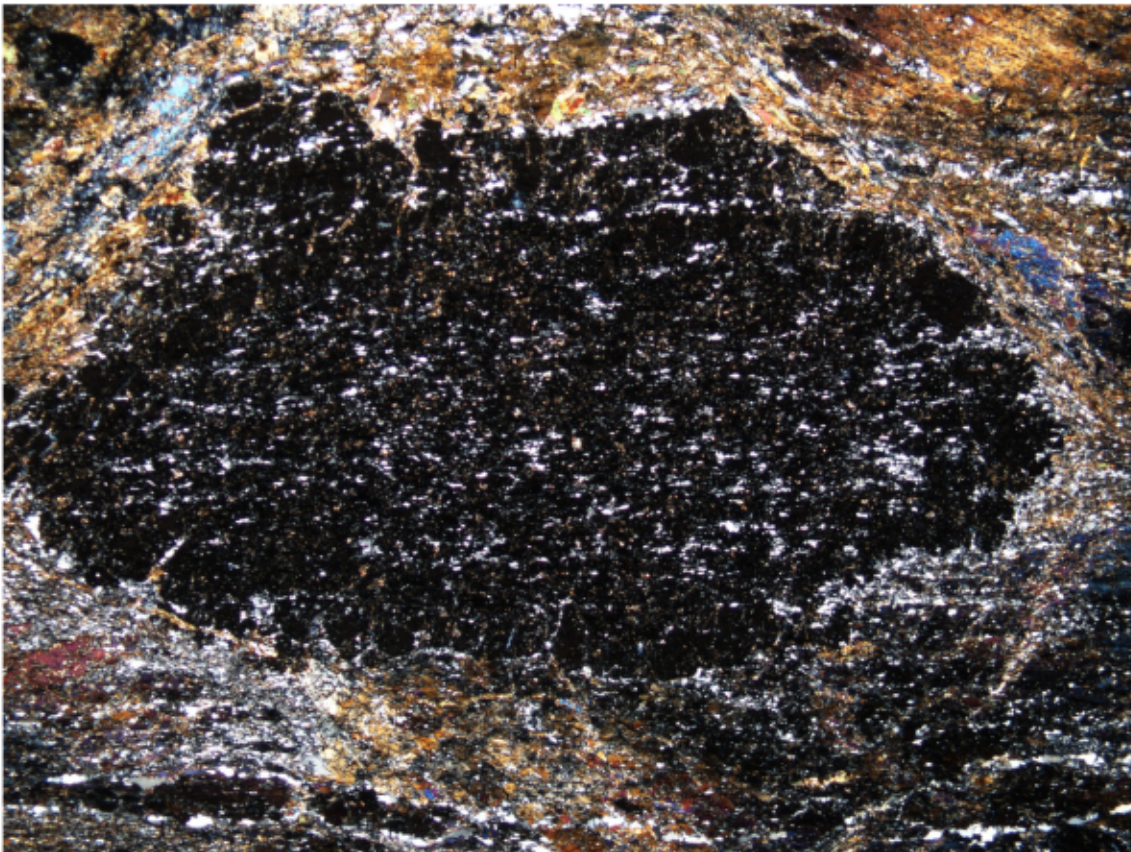




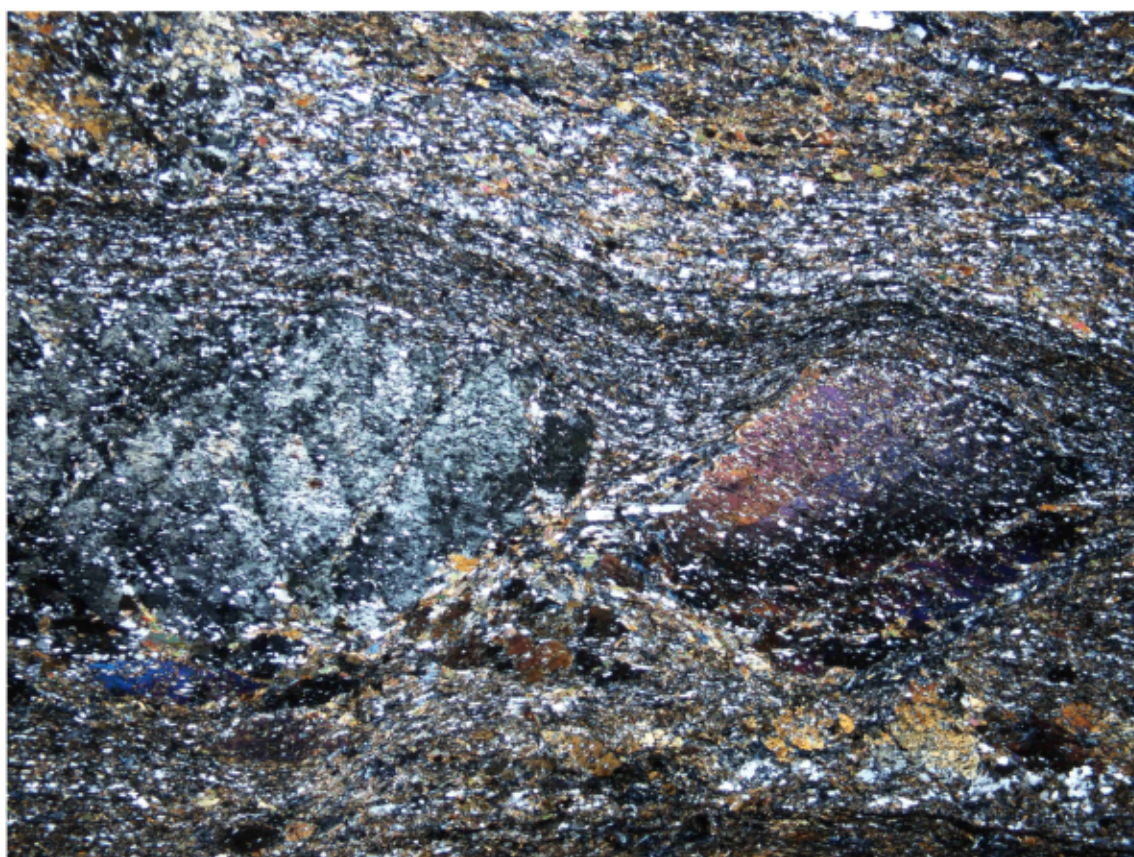




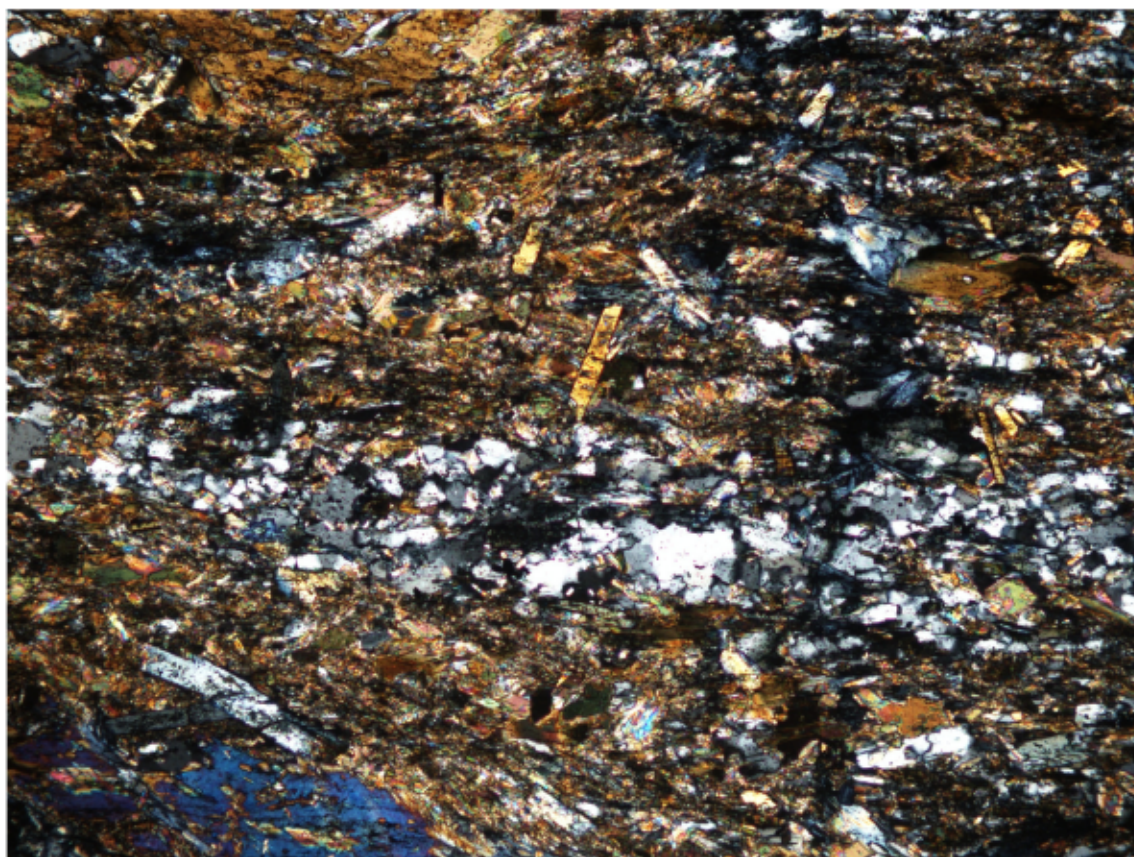
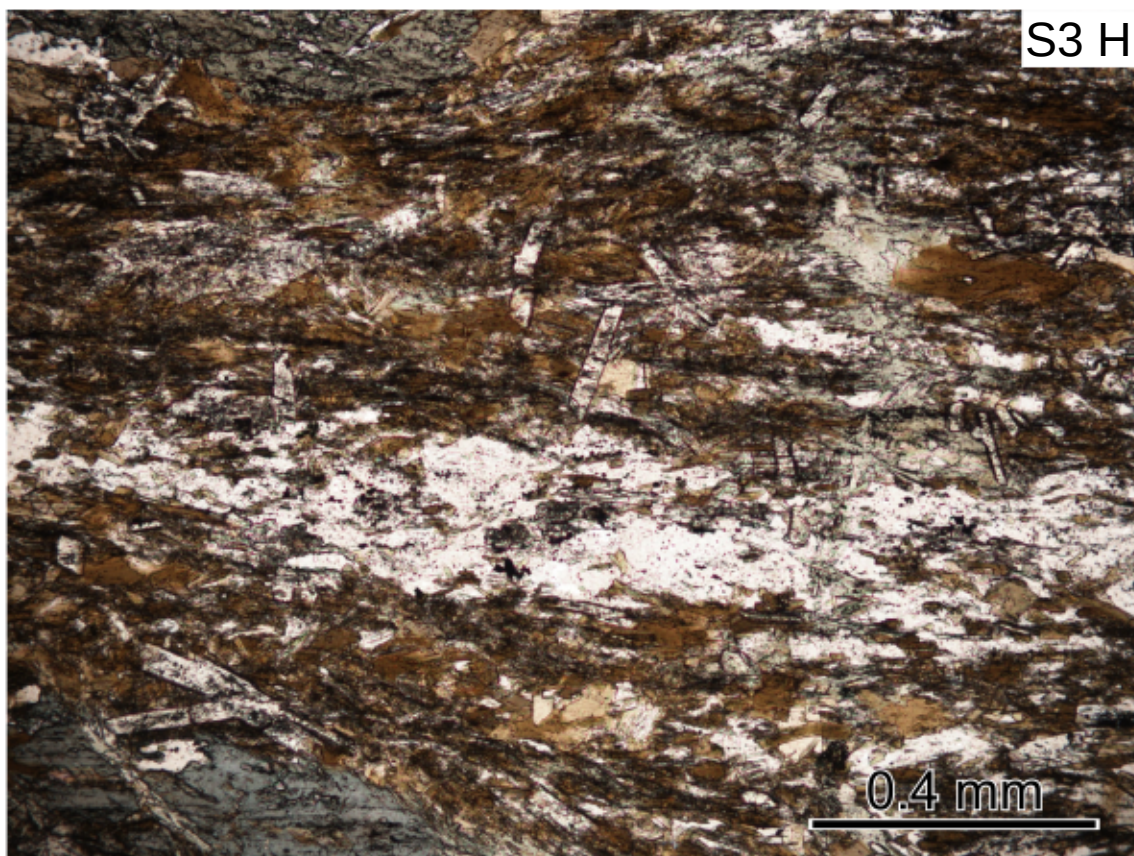




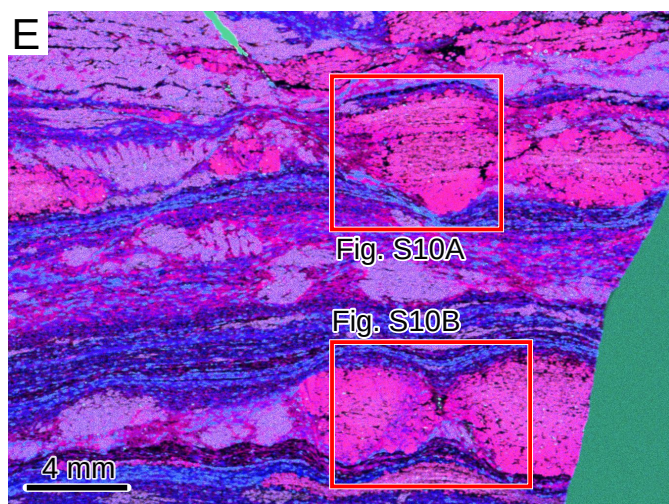
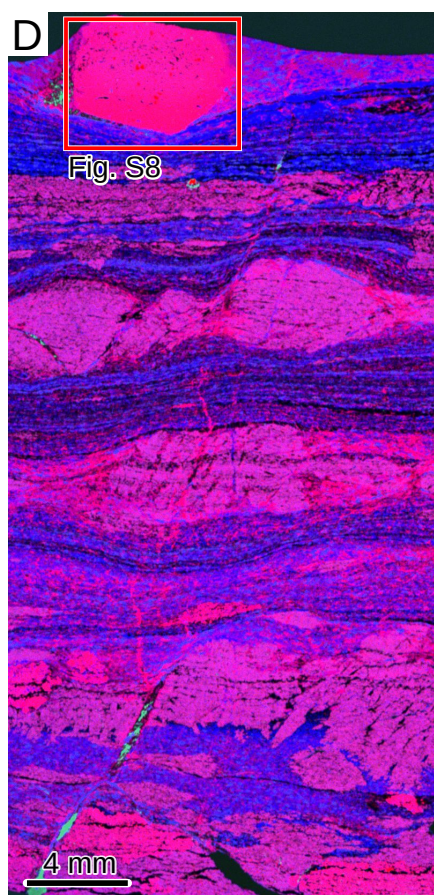
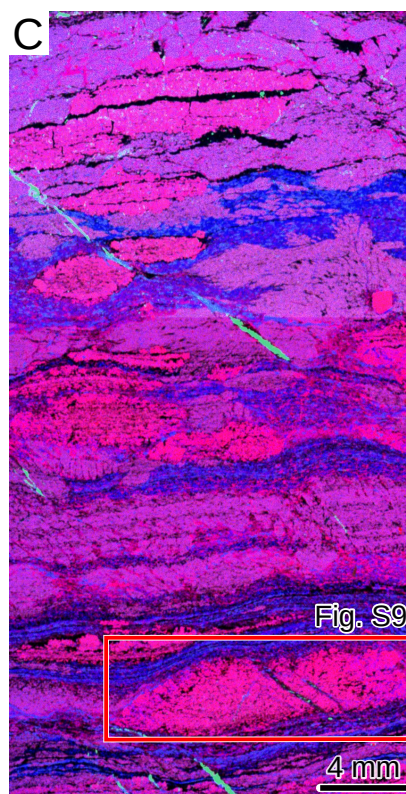
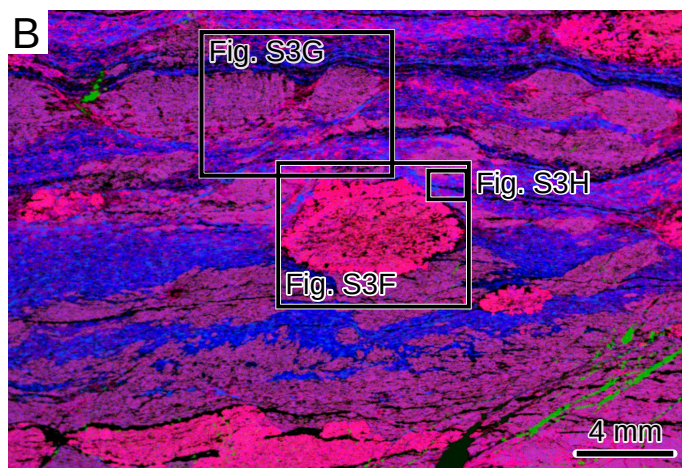
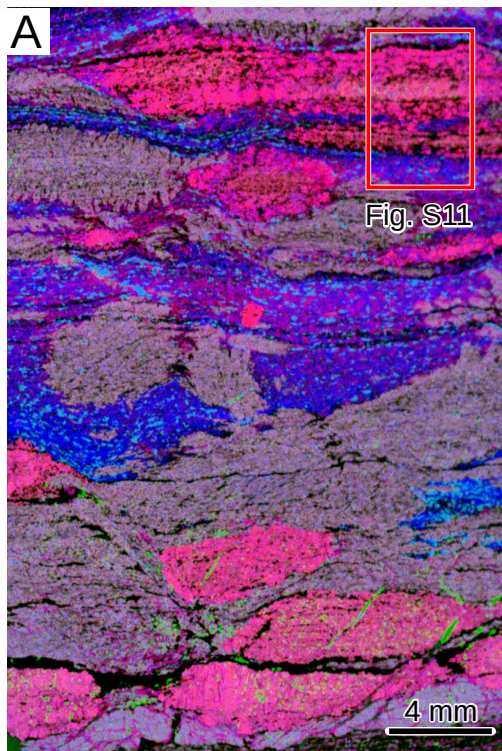












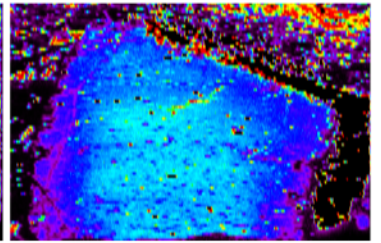
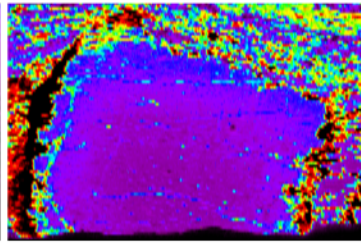
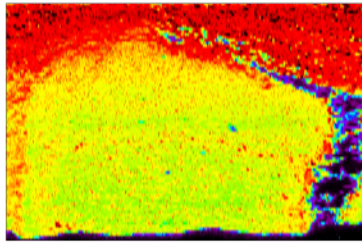
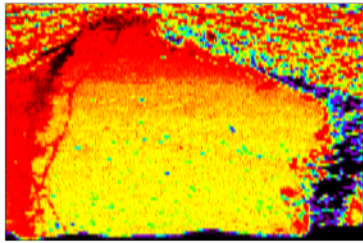


Al

Si

Mg

Ca

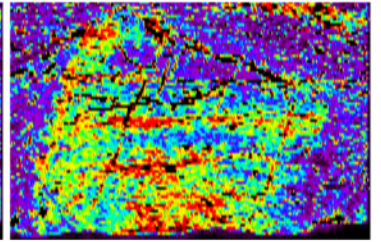
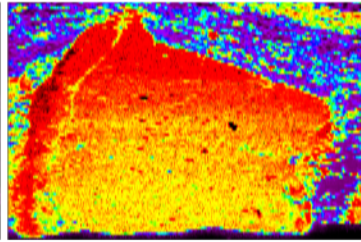
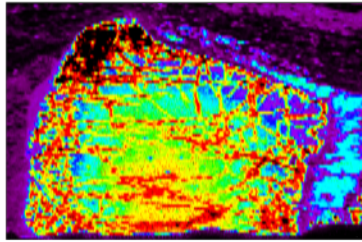
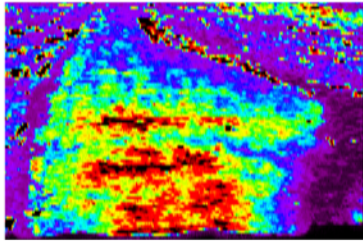


Sc

Mn

Fe

Y

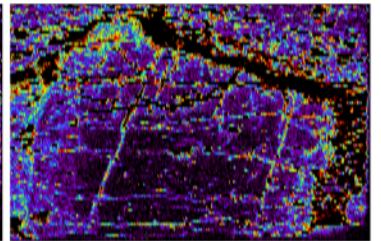
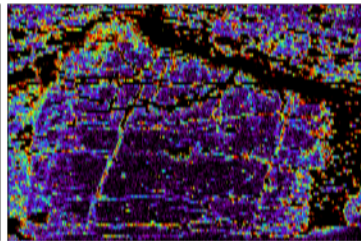
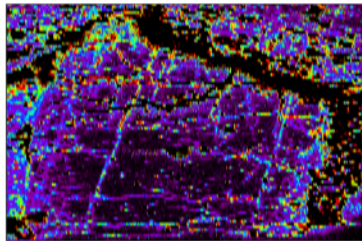
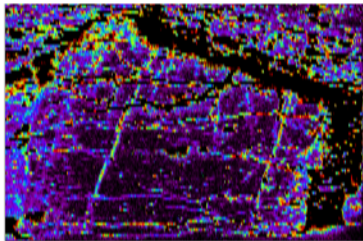


La

Ce

Pr

Nd

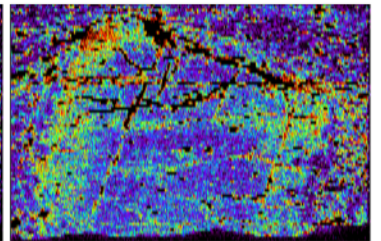
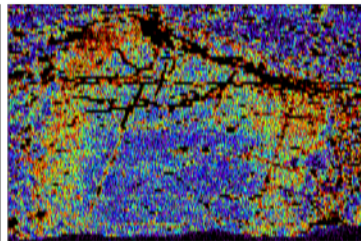
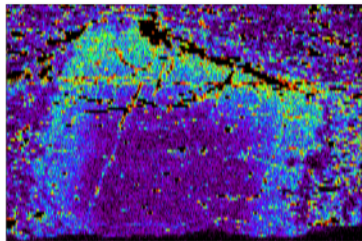
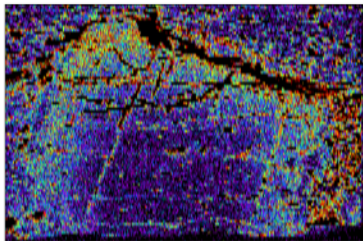


Sm

Eu

Gd

Tb

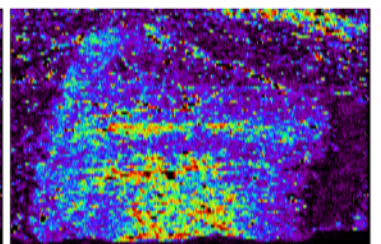
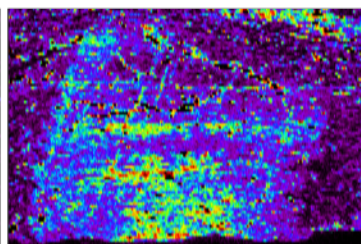
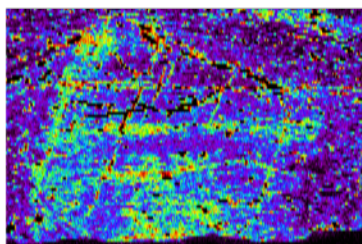
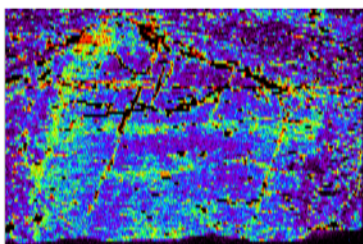


Dy

Ho

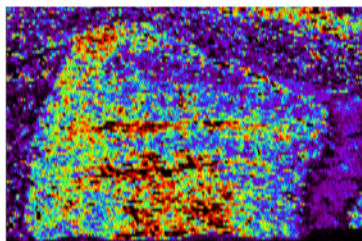
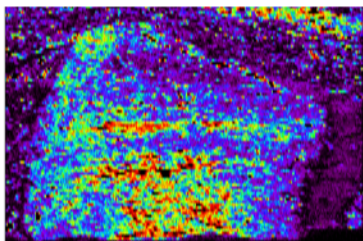
Er

Tm



Yb

Lu



Intensity

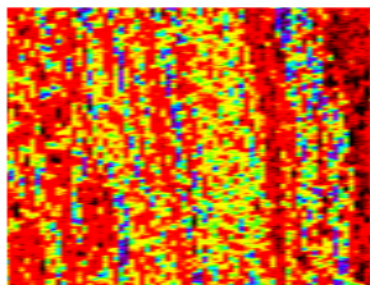
High

Low

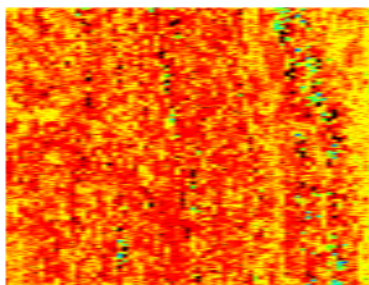




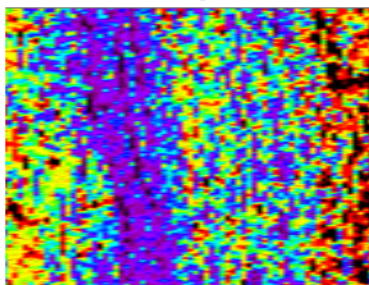
Al



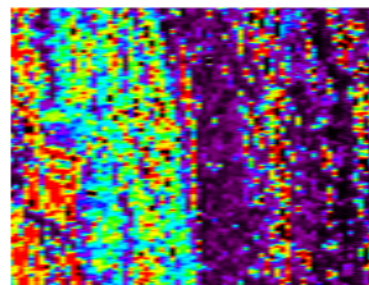
Si



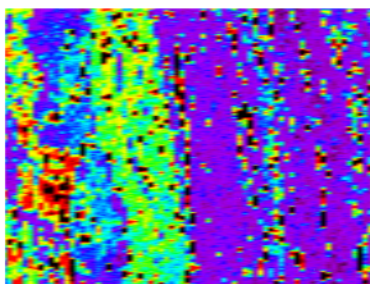
Mg



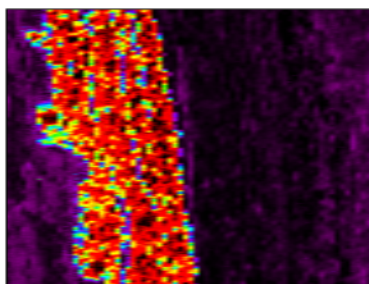
Ca



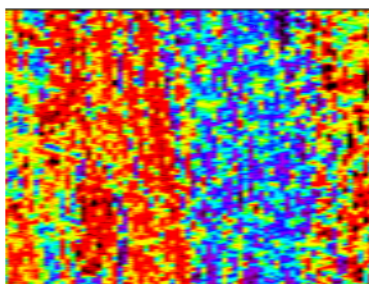
Sc



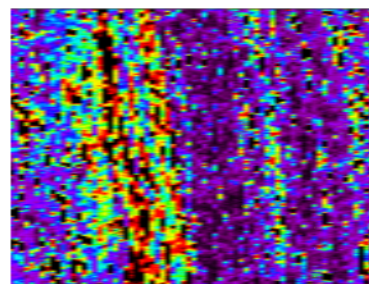
Mn



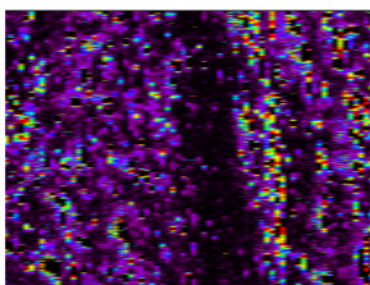
Fe



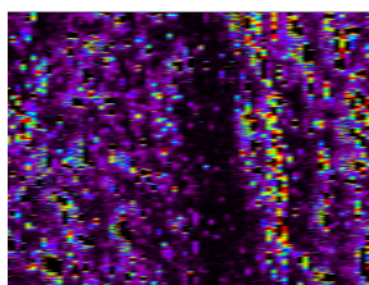
Y



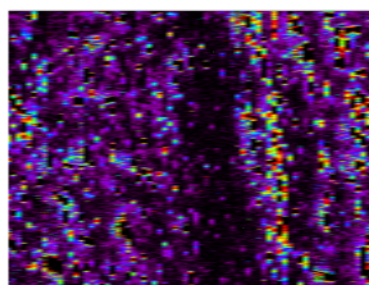
La



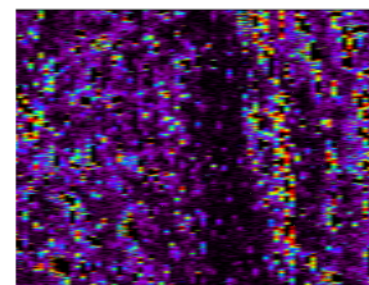
Ce



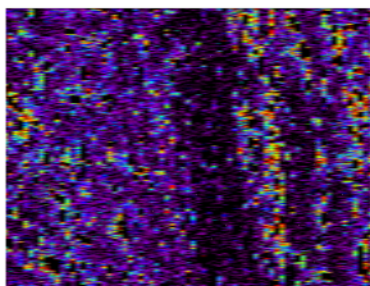
Pr



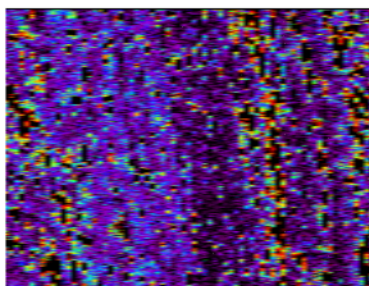
Nd



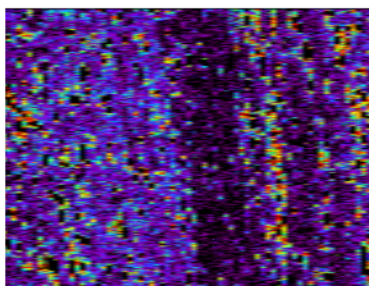
Sm



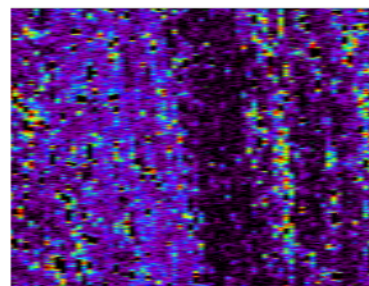
Eu



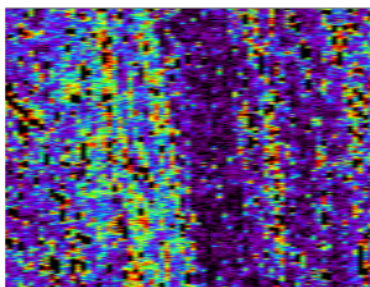
Gd



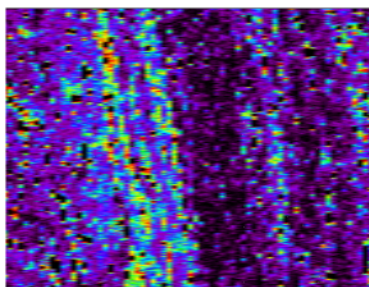
Tb



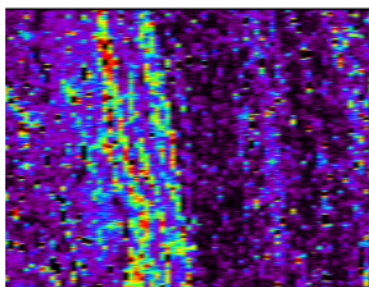
Dy



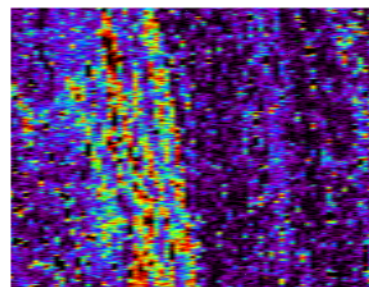
Ho



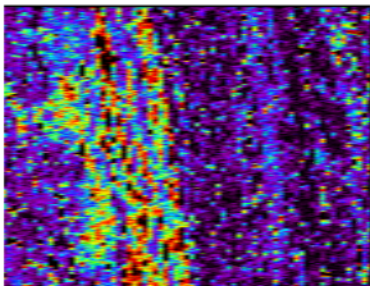
Er



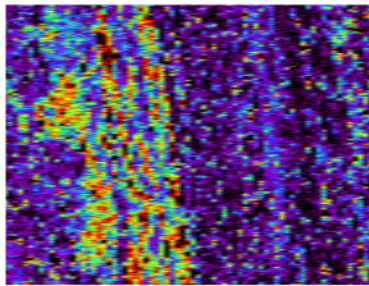
Tm



Yb



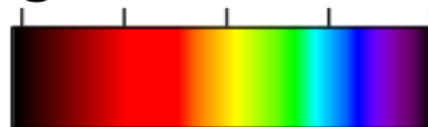
Lu



Intensity

High

Low





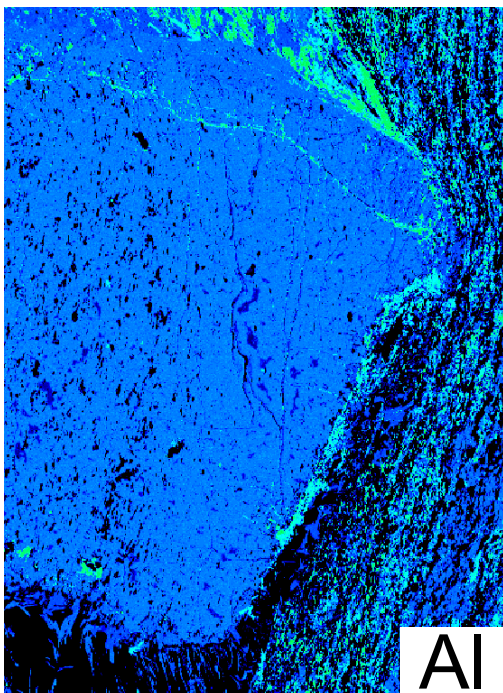
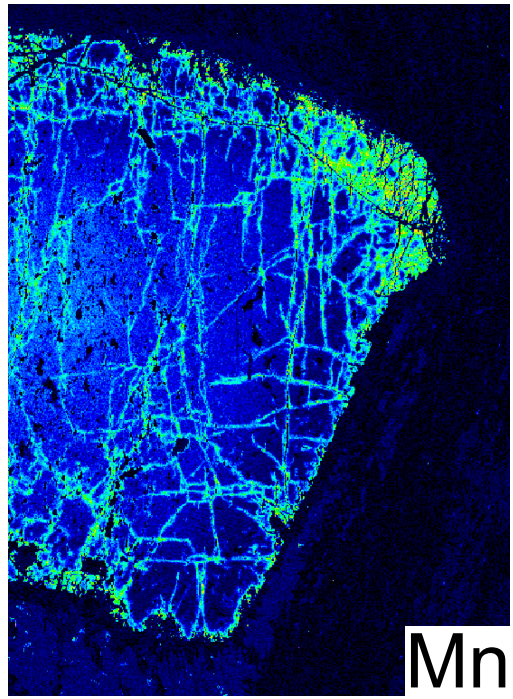
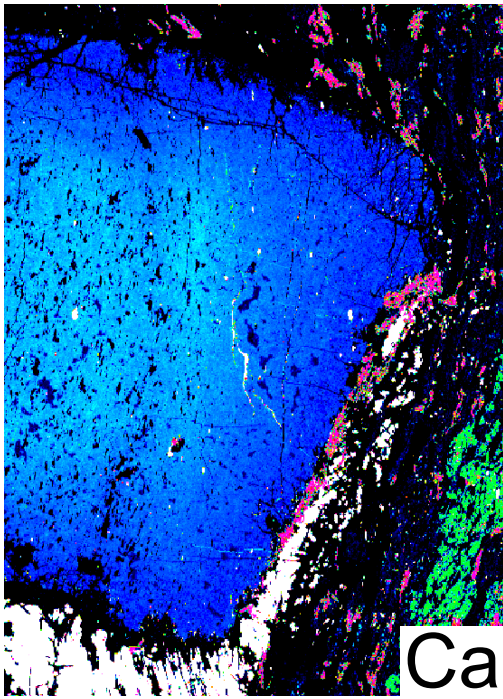
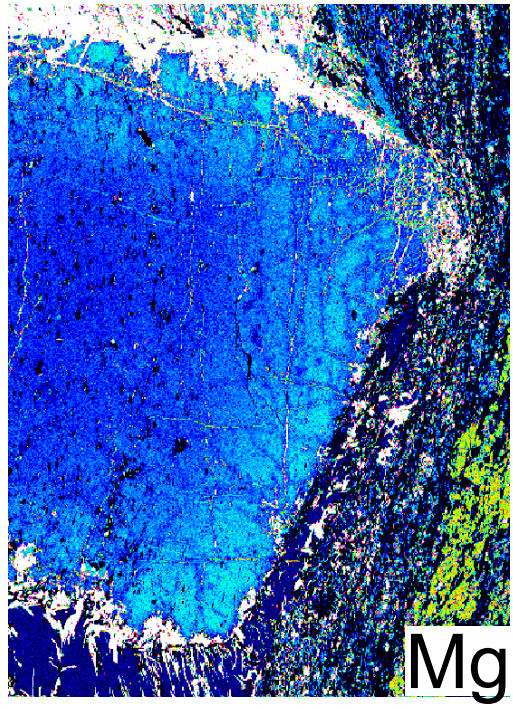
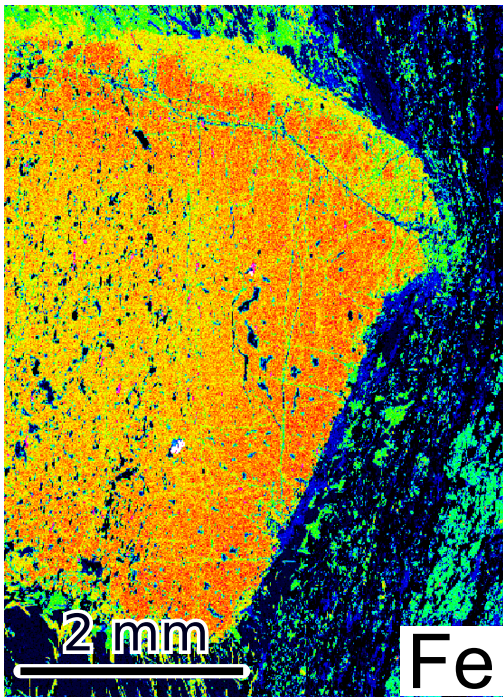




Figure S8

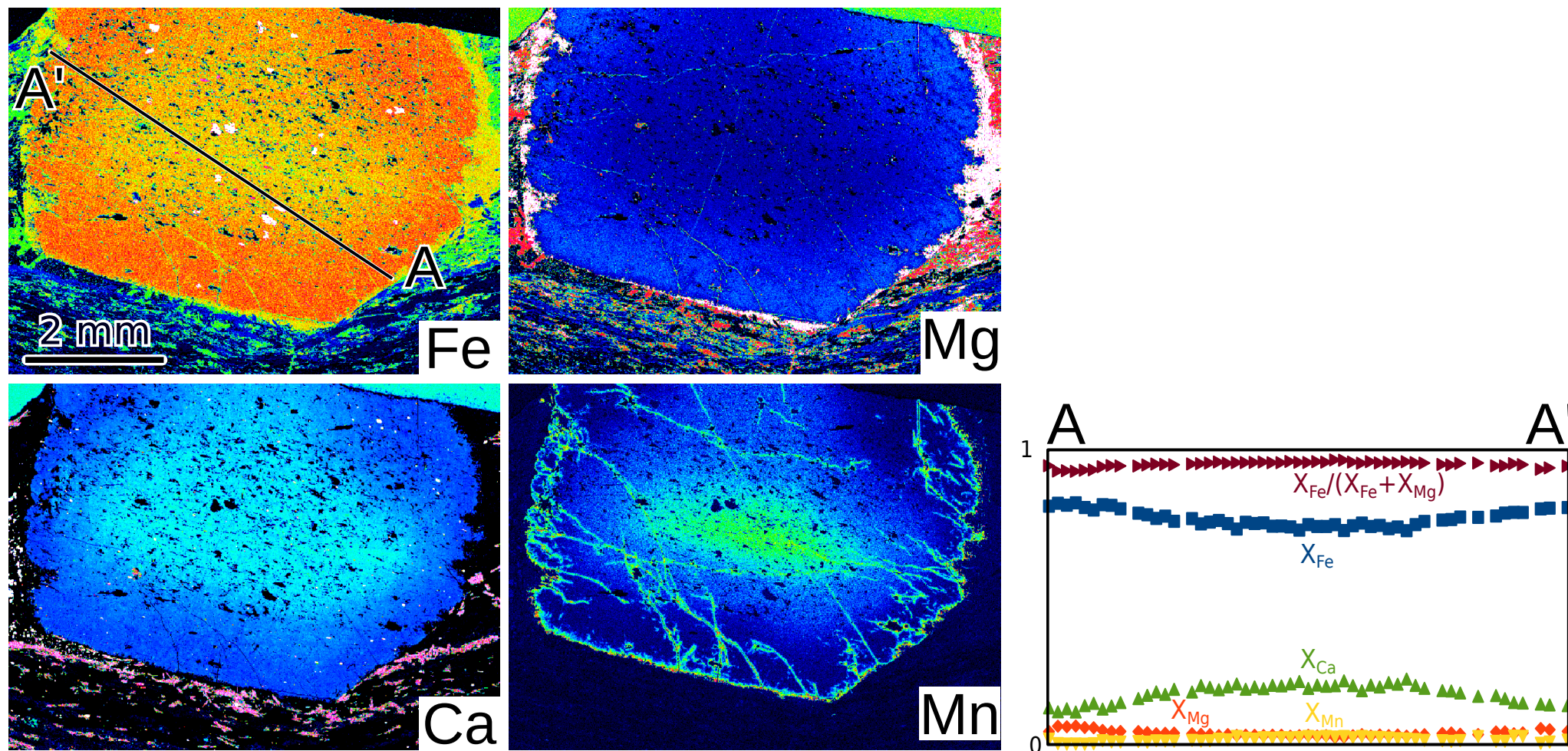




Fig. S9

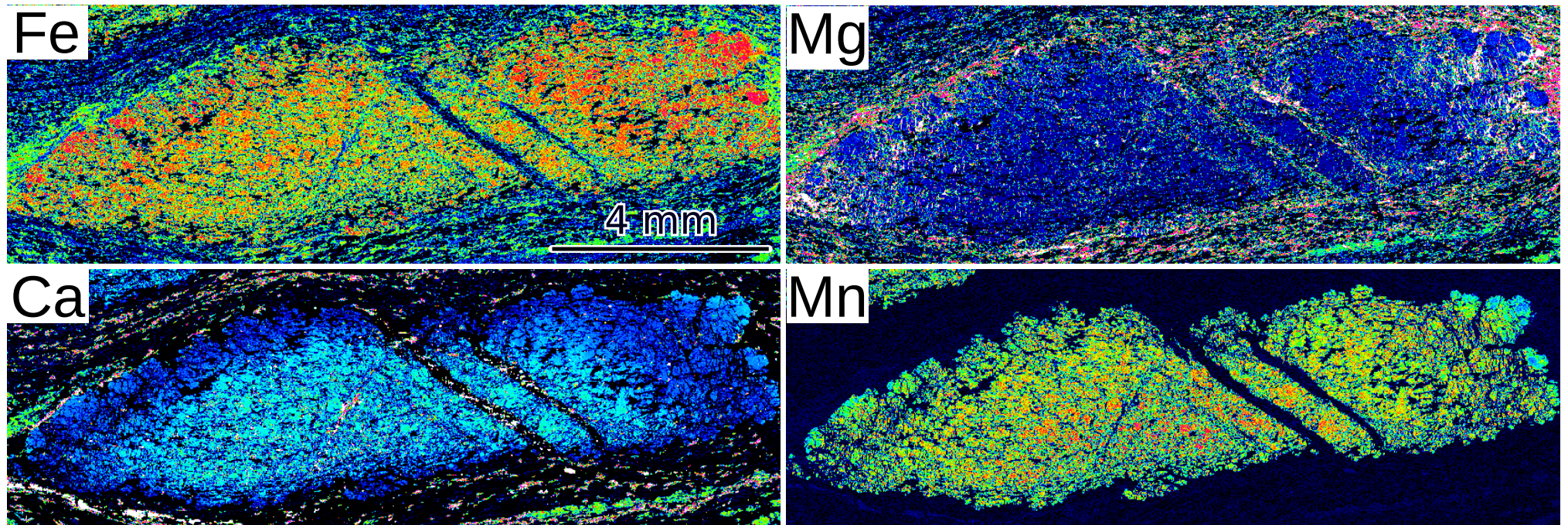




Fig. S10 A

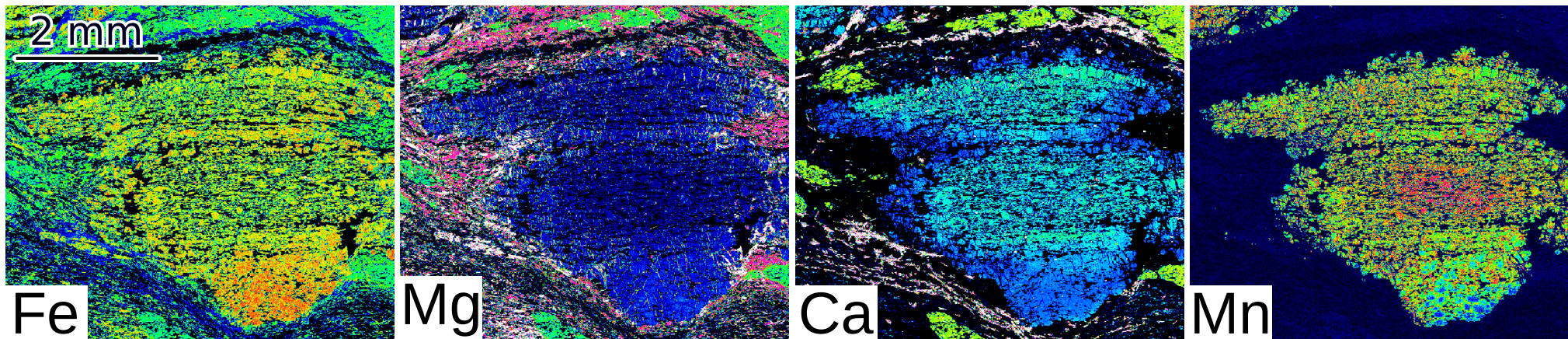
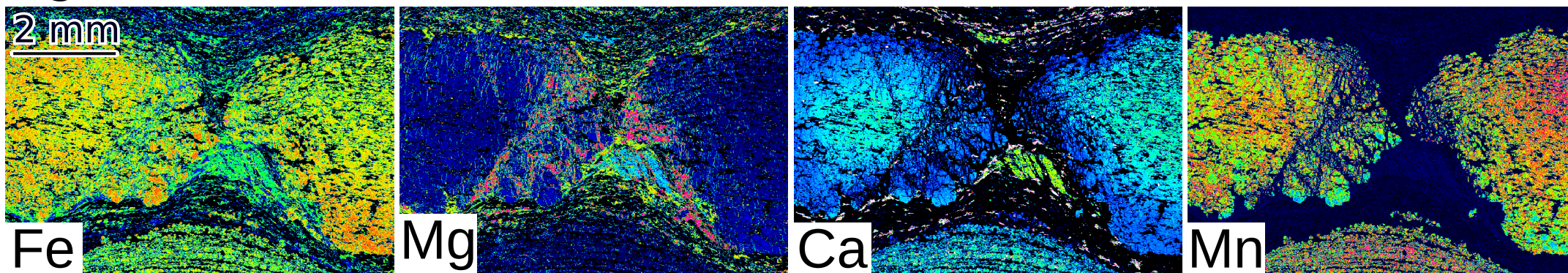


Fig. S10 B





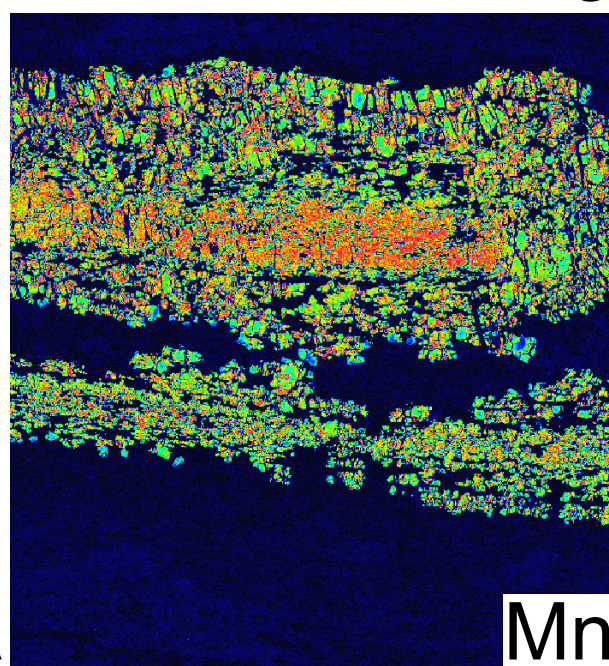
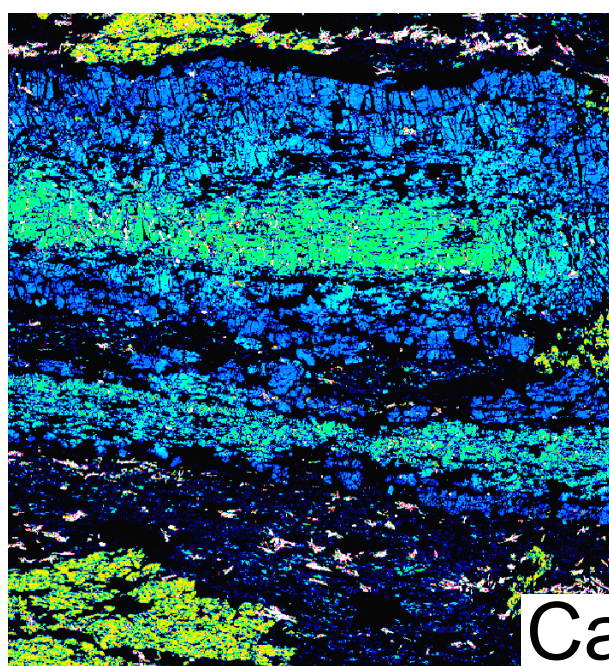
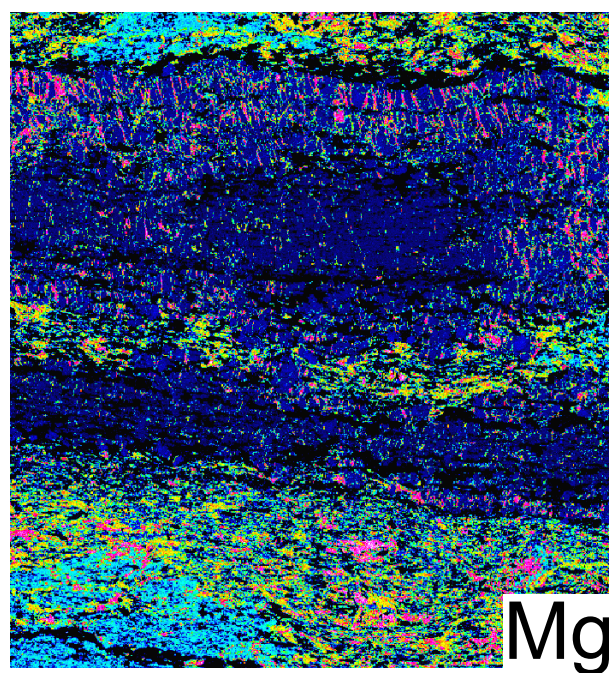
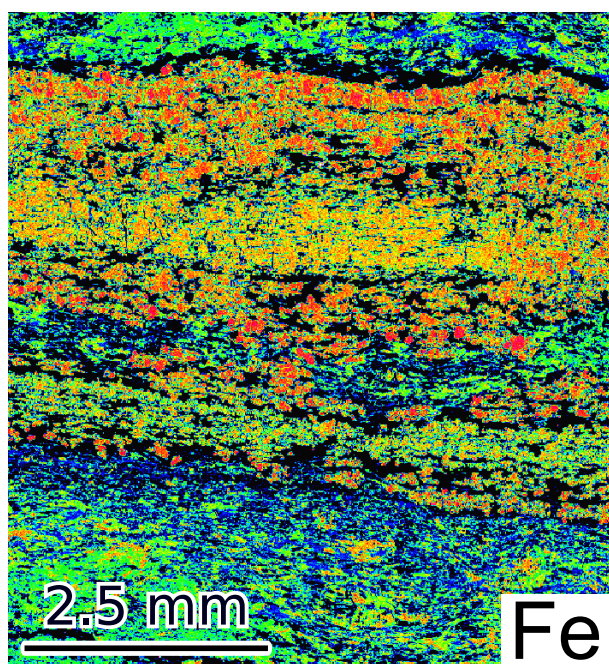
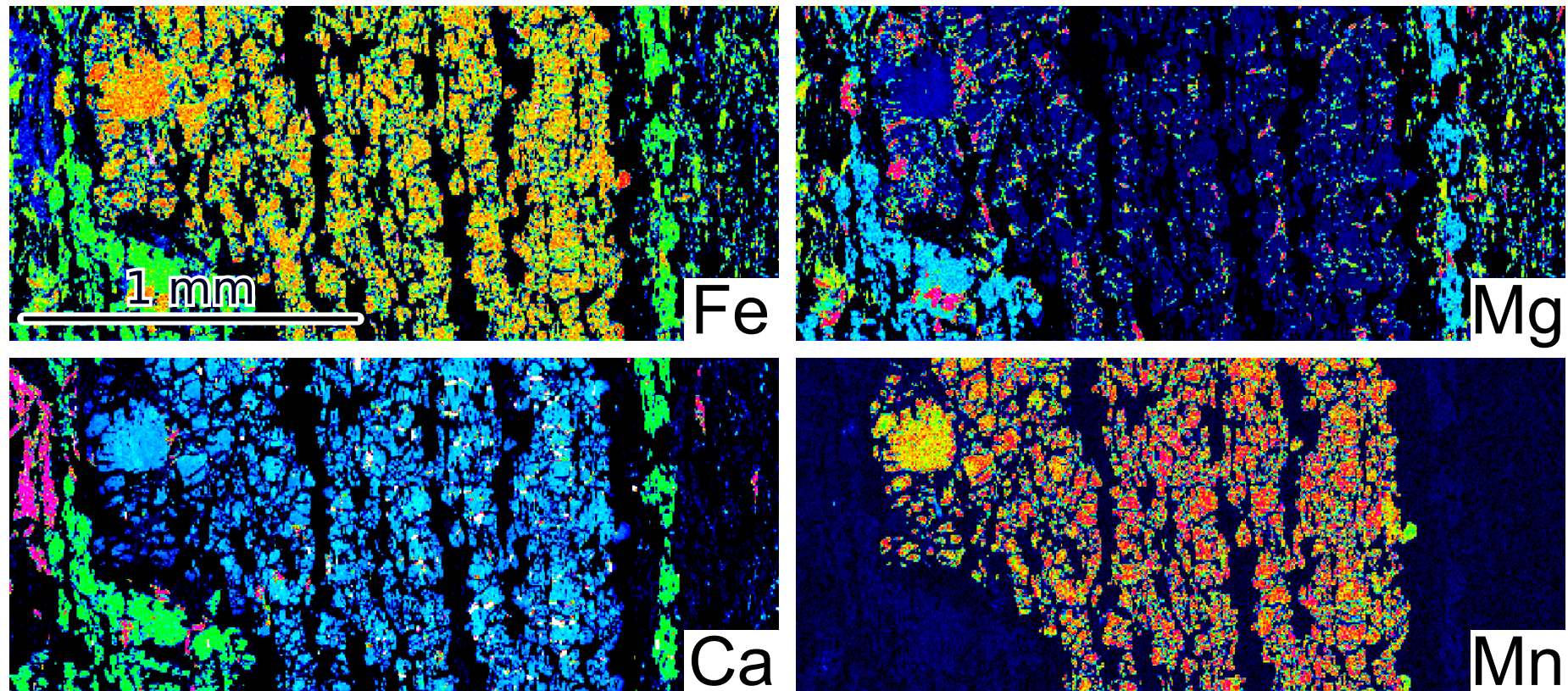




Figure S12



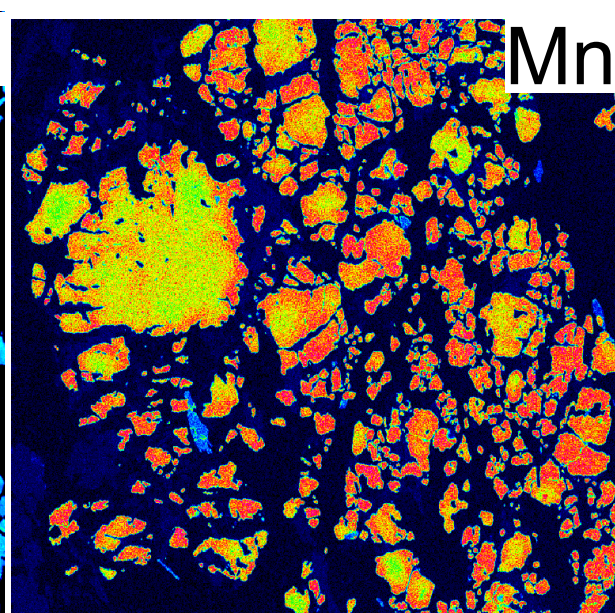
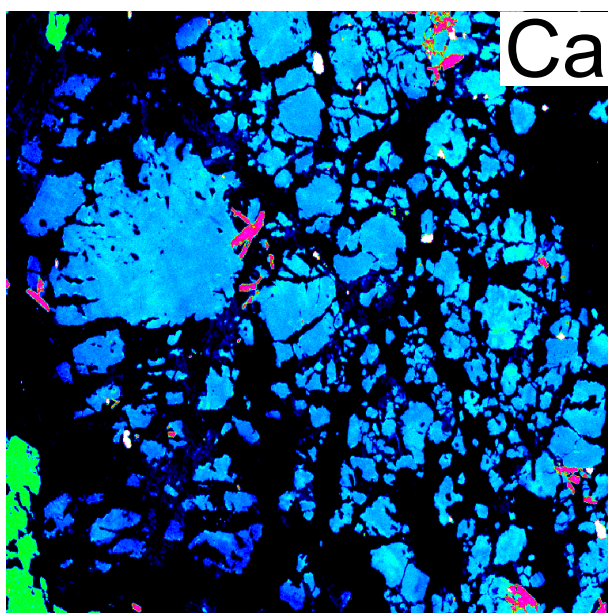
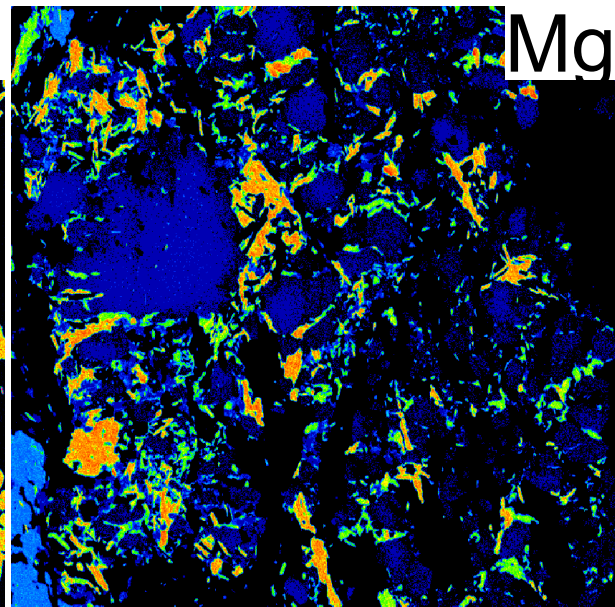
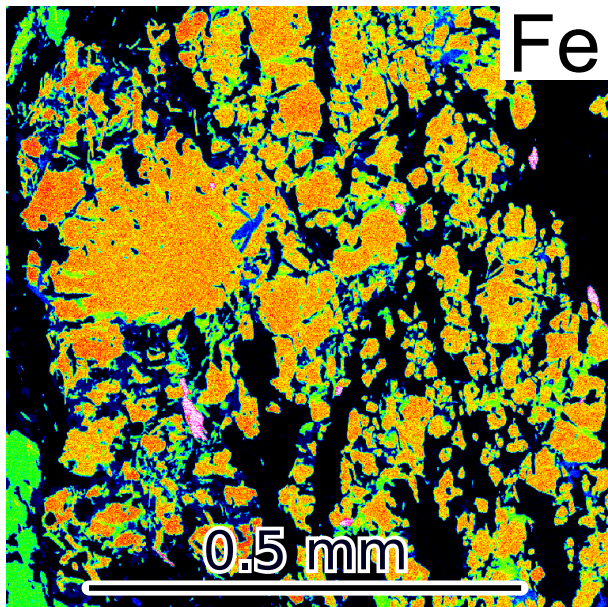
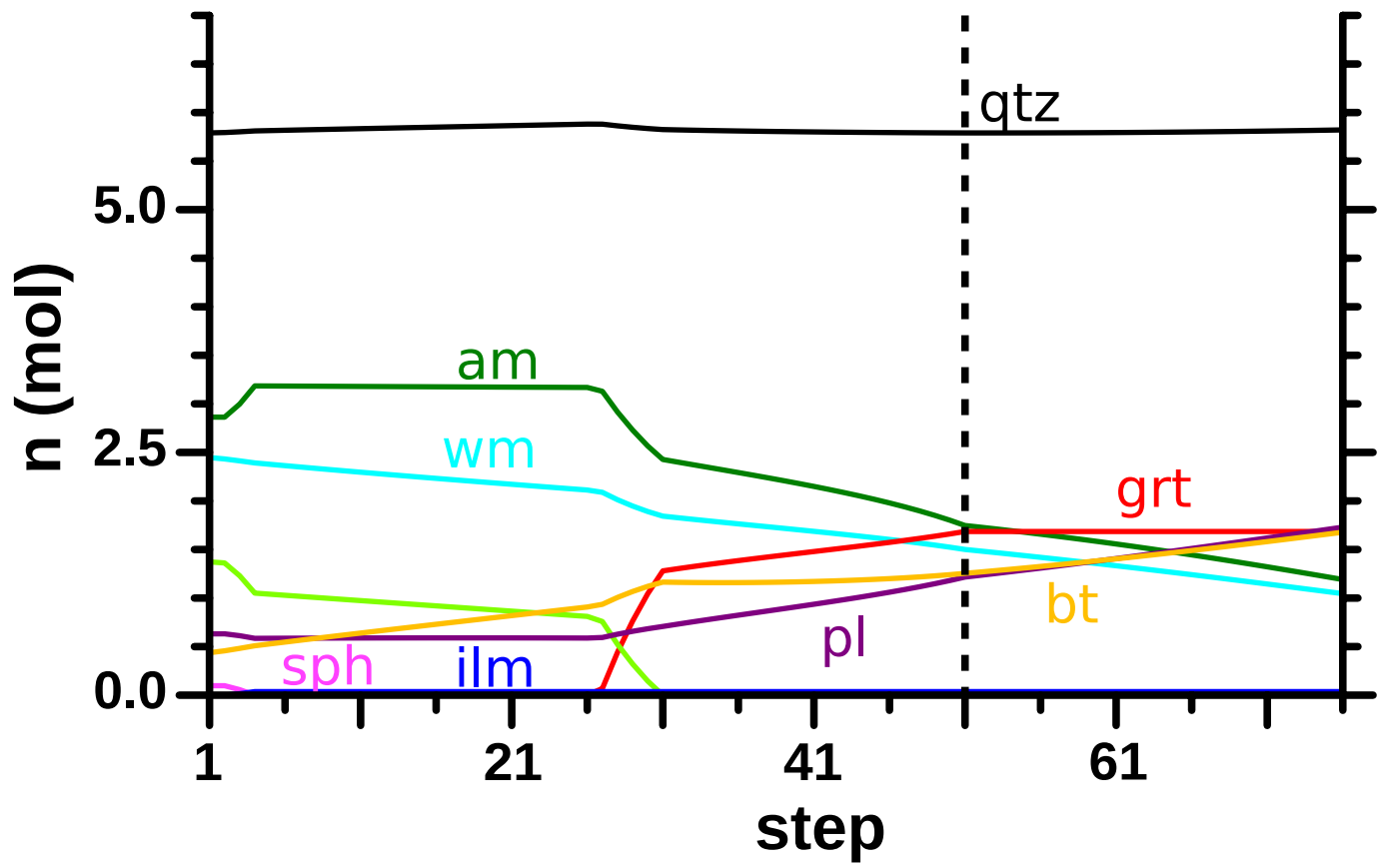
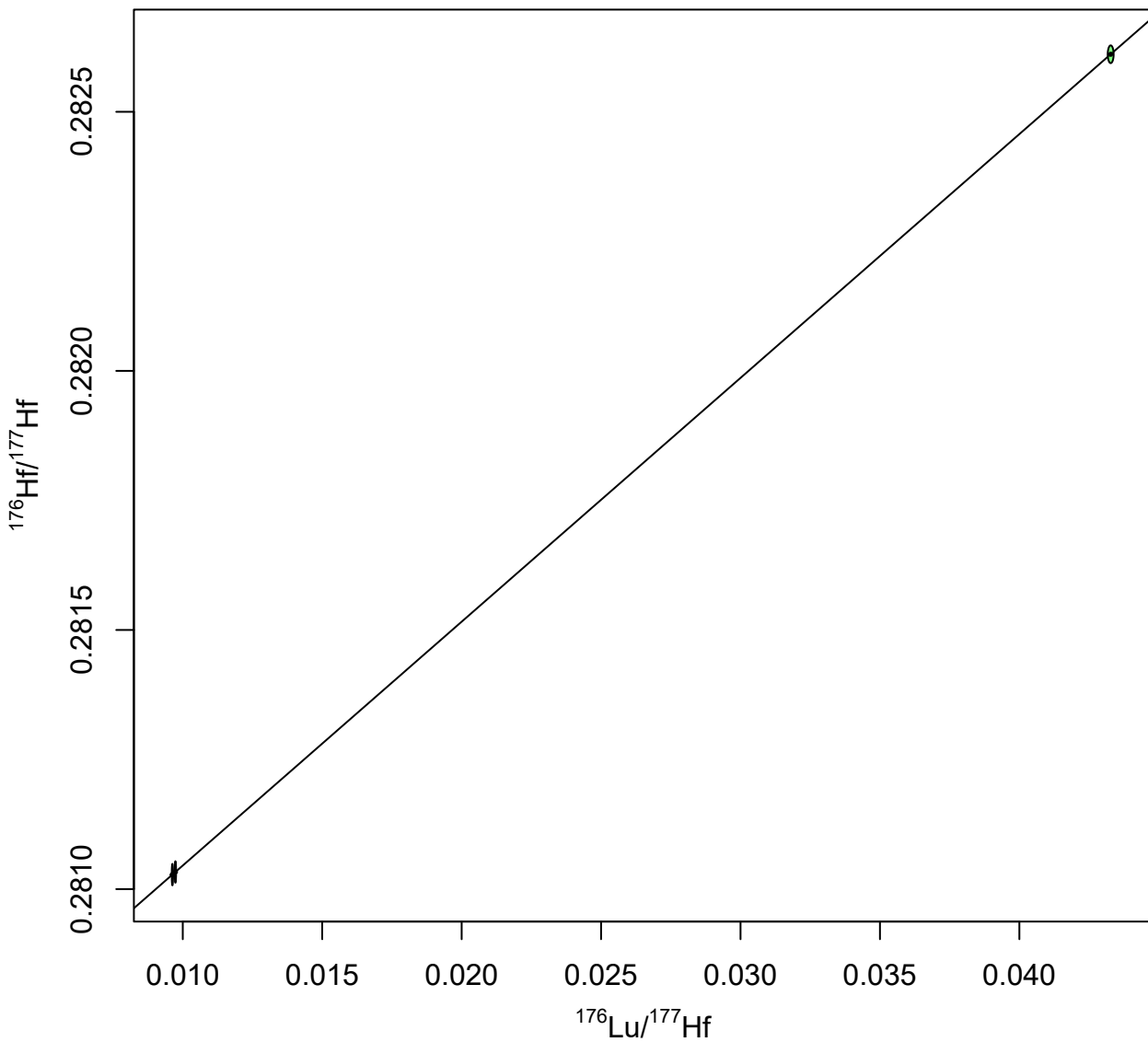


Figure S14





age =  $2462.9 \pm 30.5$  Ma (n=3)  
 $(^{176}\text{Hf}/^{177}\text{Hf})_0 = 0.280575 \pm 0.000016$   
MSWD = 0.000046



age =  $2602.9 \pm 18.1$  Ma (n=3)  
 $(^{176}\text{Hf}/^{177}\text{Hf})_0 = 0.280548 \pm 0.000014$   
MSWD = 0.00098

